

# **A Gaussian Process Emulator for Estimating the Volume of Tissue Activated During Deep Brain Stimulation**

Iván De La Pava Panche

**Director**

Álvaro Ángel Orozco Gutiérrez - MEng, PhD

**Co-director**

Óscar Alberto Henao Gallo - M.Sc, PhD



**Universidad Tecnológica de Pereira**  
**Facultad de Ingenierías Eléctrica, Electrónica, Física y Ciencias de la**  
**Computación**  
**Maestría en Ingeniería Eléctrica - Línea de automática**  
**Grupo de Investigación Automática**  
**Pereira-Risaralda**  
**2015**

# Contents

---

<b>Acknowledgements</b>	<b>2</b>
<b>Abstract</b>	<b>3</b>
<b>1 Introduction</b>	<b>4</b>
<b>2 Problem Statement</b>	<b>5</b>
<b>3 Justification</b>	<b>6</b>
<b>4 Aims</b>	<b>7</b>
4.1 General Aim . . . . .	7
4.2 Specific Aims . . . . .	7
<b>5 Background</b>	<b>8</b>
5.1 Multi-compartment neuron models . . . . .	8
5.1.1 The neuron . . . . .	8
5.1.2 The plasma membrane and the membrane potential . . . . .	9
5.1.3 Compartmental models and propagating activity . . . . .	11
5.2 Emulation of computer models . . . . .	14
5.2.1 Gaussian process classification . . . . .	15
<b>6 Materials and methods</b>	<b>17</b>
6.1 Gold standard for VTA estimation . . . . .	17
6.1.1 Electric potential propagation in the brain tissue . . . . .	18
6.1.2 Axonal distribution and VTA estimation . . . . .	18
6.2 Gaussian process emulation of the VTA . . . . .	22
6.2.1 Implementation . . . . .	22
<b>7 Results and discussion</b>	<b>25</b>
7.1 Effects of the stimulation parameters on the VTA . . . . .	25
7.2 Evaluation of the performance of the Gaussian process emulator for VTA estimation . . . . .	30
<b>8 Conclusions</b>	<b>38</b>
<b>Bibliography</b>	<b>39</b>

## Acknowledgements

---

I want to thank my family for their continuous and unconditional support during every stage of my studies, and my advisors, PhD Álvaro Ángel Orozco Gutiérrez and PhD Óscar Alberto Henao Gallo, for their help and indispensable guidance during the development of this project. I am also thankful to the MSc in Electrical Engineering program at UTP and to the Automática research group, especially to PhD Mauricio Alexander Álvarez López and PhD Genaro Daza Santacoloma for their valuable insight on several aspects of this project.

This work was funded by Colciencias under the project *Desarrollo de un sistema efectivo y apropiado de estimación de volumen de tejido activo para el mejoramiento de los resultados terapéuticos en pacientes con enfermedad de Parkinson intervenidos quirúrgicamente*, with code 1110-569-34461.

# Abstract

---

The volume of tissue activated (VTA) is a well-established approach to model the direct effects of deep brain stimulation (DBS) on neural tissue and previous studies have pointed to its potential clinical applications. However, the elevated computational time required to estimate the VTA with standard techniques used in biological neural modeling limits its suitability for practical use. The goal of this project was to develop a novel methodology to reduce the computation time of VTA estimation. To that end, we built a Gaussian process emulator. It combines a field of multi-compartment axon models coupled to the stimulating electric field with a Gaussian process classifier (GPC); following the premise that computing the VTA from a field of axons is in essence a binary classification problem. We achieved a considerable reduction in the average time required to estimate the VTA, under both ideal isotropic and realistic anisotropic brain tissue conductive conditions, limiting the loss of accuracy and overcoming other drawbacks entailed by alternative methods.

# 1. Introduction

---

Deep brain stimulation (DBS) is a surgical technique used mainly to treat movement disorders, such as Parkinson's disease, essential tremor, and dystonia, in patients whose symptoms cannot be appropriately controlled with drugs. It involves the application of electric pulses to a target region in the basal ganglia, the thalamus, or other subcortical structures, via an implanted electrode; this stimulation, when appropriately controlled, leads to symptom improvement. A fundamental step to achieve a positive therapeutic outcome, after the DBS electrode has been successfully implanted, is therefore the adequate adjustment of the stimulation parameters of the DBS device: amplitude, pulse width, frequency, and polarity of each of the conductive contacts of the electrode (cathode, anode, or inactive). The values of these parameters have to be set up in such a way that their combined effect improves the symptoms of the patient [1]. However, the process of finding an adequate parameter combination is time-consuming. It can take several painstaking sessions of trial and error adjustments, because it depends entirely on the experience of the clinical specialist with the DBS device.

Although deep brain stimulation is widely practiced, its mechanisms of action are still not completely clear, and most of the insight gained in recent years has come from computer simulations [2,3,4,5,6]. The volume of tissue activated (VTA), defined as the spatial spread of direct neural activation in response to electrical stimulation, is a measure that allows for a computational assessment of the impact of DBS [7,8,9,10]. The visualization of the VTA as part of anatomically accurate reconstructions of the brain structures surrounding the implanted electrode, has been proposed as an alternative to accelerate the process of stimulation parameters adjustment [9, 10], minimizing the adverse secondary effects that can occur if they are not adjusted carefully [1]. The standard methodology for estimating this metric consists in coupling the electric potential generated by the DBS electrode with a model of multi-compartment axons [11] arranged in a field around the electrode shaft [9]. The simulated axons that because of the stimulation fire action potentials in a one to one ratio with the DBS pulses are considered active, and their spatial distribution defines the VTA.

## 2. Problem Statement

---

As a metric that represents the extension of direct neural activation in response to the electrical stimulation, the VTA, as part of a visualization system, allows the clinical specialist to observe the brain structures that are responding directly to the delivered stimulus. Based on that information the specialist determines the possible effects that a given stimulation configuration can have on the patient. There is, however, an important hurdle in the development of practical applications for patient specific VTA visualization systems: the computation time required by the standard methodology for VTA estimation [12, 13, 14].

The gold standard for VTA estimation, that involves the computation of the brain tissue response to the electrical stimulation through a field of multi-compartment axon models [13, 15], is too computationally intensive to be used as part of a system that allows the clinical specialist to visualize, in a reasonable time, the VTA generated by a specific combination of stimulation parameters. This obstacle has led to simplified methods that minimize the use of such models by exploiting the relationship between the spatial location of the axons and the electrical stimulation. Such relationship is captured in the form of activation threshold curves, fitted from data obtained from multi-compartment axon models, that are then used to estimate the VTA [12, 15]. However, these curves do not reproduce the results of multi-compartment models accurately and cannot be applied successfully when multiple contacts of the DBS electrode are active. A possible solution to these problems is proposed in [13]. It consists in training an artificial neuronal network, with the DBS stimulation parameters as inputs and the elliptic profiles defined by the active axons as outputs. Once trained the neural network can estimate the VTA for any combination of stimulation parameters. However, this methodology only works under the assumption of isotropic tissue conductivity.

In this project, we propose an alternative approach to reduce the computational runtime of VTA estimation and overcome the limitations of the methods described above. Active axons fire an action potential for each stimulation pulse delivered by the stimulator. Inactive axons fail to respond in such a way. It follows that active and inactive axons can be thought of as part of two different classes. Furthermore, all axons are independent from one another. Under these premises, determining the volume of tissue activated from a field of axons is equivalent to a binary classification problem. The output of the standard VTA model can be then represented statistically, it can be emulated. The emulation of computer simulations circumvents the problems posed by complex and computationally intensive models by building statistical representations of them, that once obtained are used to address the issue under study without additional runs of the original simulation. The main approach to developing emulators uses Gaussian processes [16, 17]. Our goal was then to train a Gaussian process classifier (GPC) to determine whether an axon at a given position in space was active due to DBS, and by doing so, to estimate the VTA.

### 3. Justification

---

The gold standard for the estimation of the volume of tissue activated in deep brain stimulation, while biophysically accurate, is too computationally intensive for practical applications. Common alternatives found in the literature, such as activation threshold curves, present an array of shortcomings: they can produce large errors when compared with the gold standard, they work only for a limited range of stimulation parameters, or they are based on strong ideal assumptions [12, 13, 15]. The development of a novel approach that can reduce the computation time for VTA estimation, and reproduce the results of the gold standard accurately across the universe of possible combinations of stimulation parameters under realistic assumptions, would be an important step forward towards practical applications for patient specific VTA visualization systems. Besides, the development of this project will contribute to the ever-expanding world of computational bioengineering, through the combination of a well-established methodology to model the effects of extracellular stimulation on neural fibers with machine learning techniques, specifically with a binary classifier based on Gaussian processes.

## 4. Aims

---

### 4.1 General Aim

To develop a methodology to estimate the volume of tissue activated during deep brain stimulation that reduces the computation time when compared with the gold standard.

### 4.2 Specific Aims

- To implement the gold standard for VTA estimation. Namely, a field of multi-compartment myelinated axons that respond to an extracellular electric stimulation waveform propagating in a tissue medium whose conductivity can be assumed as either isotropic or anisotropic.
- To implement a Gaussian Process emulator, based on Gaussian Process classification, in order to reduce the computation time required for VTA estimation.
- To validate the results obtained from the emulator by direct comparison with the gold standard, through an error metric, for a set of stimulation configurations relevant in the context of DBS.

## 5. Background

---

### 5.1 Multi-compartment neuron models

#### 5.1.1 The neuron

Neurons are the functional units of the nervous system. These cells receive, process and propagate electrical signals through changes in the electric potential across their plasma membranes. The excitable nature of their membranes allows the potential across them to undergo linear and non-linear changes in response to stimuli of varying intensity. When the electrical stimulation is above threshold an all-or-nothing transient depolarizing spike in membrane potential, known as an action potential, is triggered. Action potentials are responsible for representing and transmitting information in the nervous system.

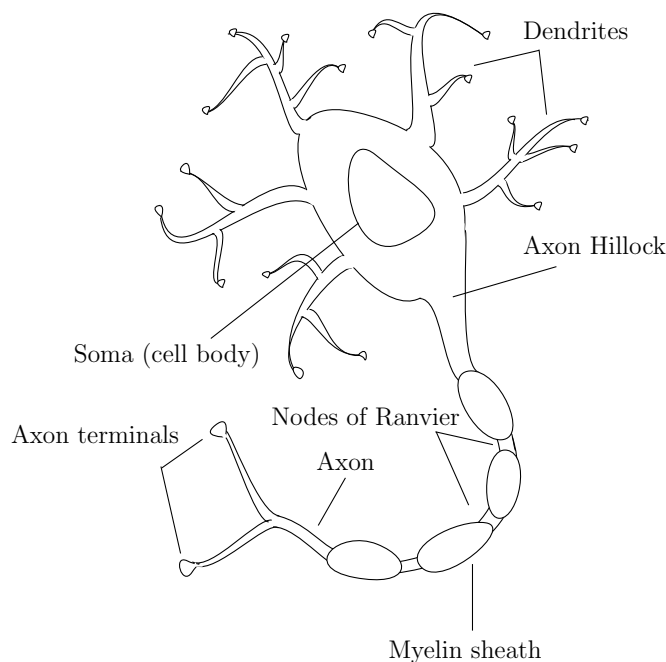


Figure 5.1: Scheme of the structural features of an idealized neuron.

The structural features of an idealized neuron include the dendrites, the soma or cell body, the axon, the axonal terminals, myelination, and the nodes of Ranvier (Figure 5.1). The dendrites form synapses with upstream neurons, receive information from them and propagate it to the soma, where it is processed. The integration of signals arriving to the soma takes place in a location called axon hillock. If as a result of the

incoming signals an action potential is fired, it will propagate down the axon towards the axon terminals which synapse with the dendrites of downstream neurons. Many axons are covered by sheaths of myelin that work as insulators and speed up signal conduction. The nodes of Ranvier are highly excitable spots, because of their high density of voltage gated ion channels, between the sheets of myelin. They regenerate the action potential, making action potential propagation in myelinated axons saltatory [18, 19, 20]

### 5.1.2 The plasma membrane and the membrane potential

The cell membrane, or plasma membrane, consists of a phospholipid bilayer with embedded proteins. Each layer of lipids is oriented so that their polar groups (hydrophilic) are in contact with the intracellular and extracellular aqueous mediums. Their non-polar tails (hydrophobic) face one another, forming a barrier impermeable to water soluble molecules, such the electrolytes or dissolved ions present in the intracellular and extracellular spaces. The differing ion concentrations at each side of the membrane create a charge imbalance that translates into a potential difference across the membrane  $V_m$

$$V_m = V_{in} - V_{out} \quad (5.1)$$

where  $V_{in}$  and  $V_{out}$  are the electric potentials of the intracellular and extracellular mediums, respectively.  $V_m$  is static in non-excitable cells and dynamic in excitable cells such as neurons, cardiac myocytes and pancreas beta cells [18]. The presence of two conductor materials, the electrolytes of the extracellular and intracellular mediums, separated by an insulator, the phospholipid bilayer, also gives rise to a cell membrane capacitance  $C_m$ . When there is a change in voltage across the membrane ions redistribute at each side of it and produce a capacitive current  $I_C$

$$I_C = C_m \frac{dV_m}{dt}$$

The membrane bound proteins form channels and pumps that allow for a regulated transport of ions and other water soluble molecules across the membrane. This flow of charged molecules across the membrane, in response to electrochemical gradients, creates a resistive current  $I_R$  proportional to the membrane conductance  $G_m$

$$I_R = G_m V_m$$

### Equivalent circuit representation

For an idealized isopotential cell, or for a small enough patch of membrane, the passive electrical behavior of the membrane can be represented by an RC circuit subject to a potential difference equal to  $V_m$  (Figure 5.2). Kirchhoff's current law states that the total current, the capacitive current and the resistive current, must sum to zero. This leads to a differential equation for the membrane potential

$$0 = I_C + I_R = C_m \frac{dV_m}{dt} + G_m V_m \quad (5.2)$$

In equation 5.2  $I_R$  represents the total flow of different ionic species across the membrane through highly specific ion channels. A more accurate cell membrane model includes instead explicit representations of the ionic currents crossing the membrane, as well as possible sources of external stimulation. Figure 5.3 shows a circuitual model of the cell membrane with a series of parallel conductances, one per each ionic species ( $x_1, x_2, x_3$ ), and their corresponding equilibrium potentials ( $E_{x_1}, E_{x_2}, E_{x_3}$ ), that is, the electric potential at which there is not net flow of ions for that species. The electric force experienced by an ion is proportional

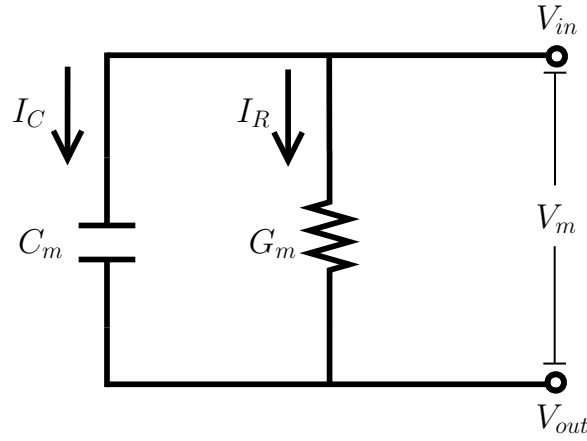


Figure 5.2: RC circuit that represents the passive electrical behavior of a small membrane patch.

not to the membrane potential  $V_m$ , but to  $V_m$  minus its equilibrium potential. The equilibrium potential for each ion is computed from Nernst equation, a function of the ionic concentrations at each side of the membrane [20].  $I_m$  represents the total current crossing the membrane, e.g. a stimulus in the form of a current injection to the interior of the cell.

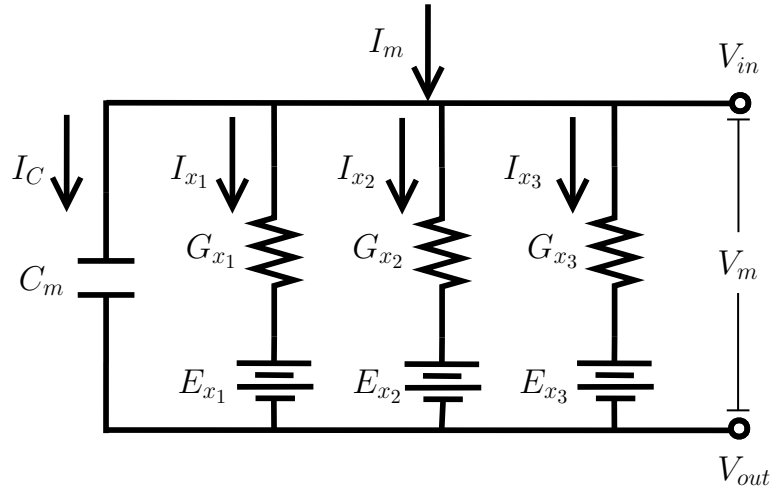


Figure 5.3: Circuit model of a membrane patch with a series of parallel conductances and batteries, representing the different ionic species ( $x_1, x_2, x_3$ ) considered in the model and their corresponding equilibrium potentials ( $E_{x_1}, E_{x_2}, E_{x_3}$ ).

For  $n$  ionic species, from Kirchhoff's current law we obtain that

$$C_m \frac{dV_m}{dt} = I_m - I_{ion} \quad (5.3)$$

$$I_{ion} = \sum_{i=1}^n G_{x_i} (V_m - E_{x_i})$$

Equation 5.3 allows for the computation of the time evolution of  $V_m$  when the membrane is passive. Active membrane behavior, including the occurrence of action potentials, can only be explained by accounting for non-linear variations in the membrane permeability to different ions. The presence of voltage gated ion channels in excitable cells leads to non-linear changes in the amount of channels open to specific ionic species in response to changes in the membrane potential. It follows that the conductances  $G_{x_i}$  are, in general, non-linear functions of  $V_m$ . Figure 5.4 shows a circuit membrane model with two non-linear conductances, for  $Na^+$  and  $K^+$  ions, and a constant leakage conductance. The circuit diagram corresponds to the Hodgkin-Huxley model of neuronal excitation of the squid giant axon.

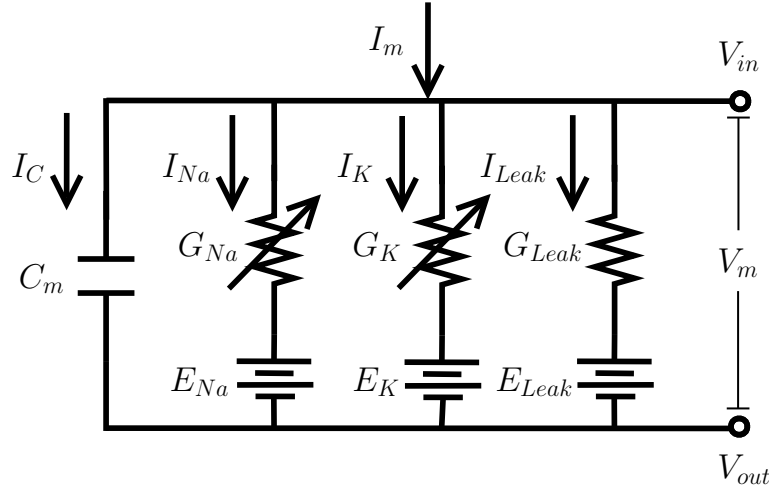


Figure 5.4: Circuit diagram of the Hodgkin-Huxley model of neuronal excitation of the squid giant axon.

Modifying equation 5.3 to include the voltage dependence of the ionic conductances, and normalizing all units we obtain

$$c_m \frac{dV_m}{dt} = i_m - i_{ion} \quad (5.4)$$

$$i_{ion} = \sum_{i=1}^n g_{x_i}(V_m)(V_m - E_{x_i})$$

where  $c_m$ ,  $g_{x_i}$ ,  $i_{ion}$ , and  $i_{stim}$  are equal to  $C_m$ ,  $G_{x_i}$ ,  $I_{ion}$ , and  $I_m$  divided by the surface area of the cell or patch of membrane under study, respectively. The use of specific units instead of absolute units is a common practice in biological cell modeling since it allows for the comparison of membrane properties between cells of different sizes and shapes. The functional relations between the ionic conductances and the membrane potential  $g_{x_i}(V_m)$  can be modeled using the Hodgkin-Huxley formalism [21].

### 5.1.3 Compartmental models and propagating activity

Equation 5.4 describes the temporal behaviour of  $V_m$  in an isolated, isopotential patch of membrane (or in a whole cell membrane under space-clamp conditions). To model the interaction between an electric field, like that generated during DBS, and nearby neural structures it is also necessary to consider how voltage spreads across the membrane, to describe the spatial behaviour of  $V_m$ . This can be achieved using multiple

connected RC circuits, in an approach known as compartmental modeling.

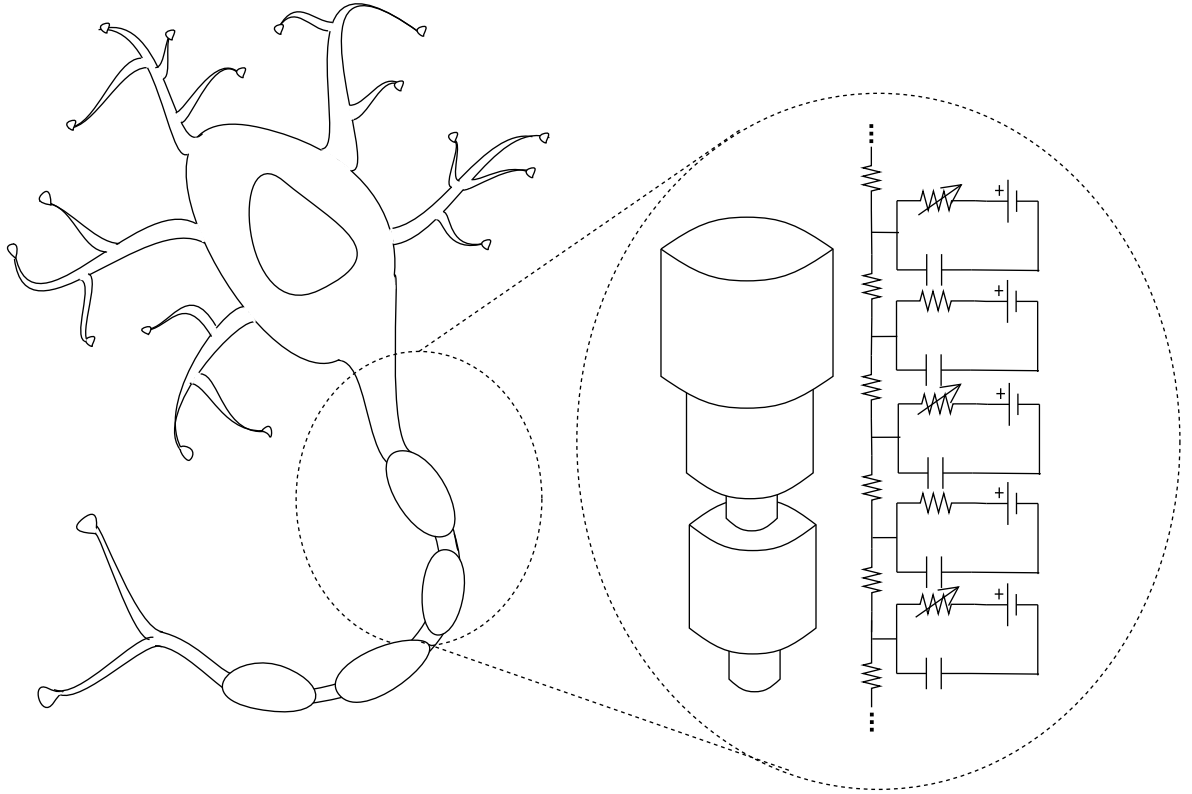


Figure 5.5: In multi-compartment neuron models the neuron's morphology is represented by simple geometrical objects, such as spheres or cylinders, that are in turn associated to circuit models of the membrane electrical behaviour.

In a compartmental, or multi-compartment model a neuron is represented as many isopotential membrane patches connected by resistors. Each membrane patch is associated with a simple geometrical object, like a sphere or cylinder, that correspond to a specific region of the neuron's morphology (Figure 5.5). Specific membrane properties together with the compartments' surface areas and cross-sectional areas can be readily translated to the capacitances and conductances of the model's circuitual representation [22].

Figure 5.6 shows a circuit diagram of a non-branched multi-compartment model. From from Ohm's law

$$r_i \Delta x I_a(x, t) = V_{in}(x, t) - V_{in}(x + \Delta x, t)$$

where  $r_i$  is the intracellular axial resistance per unit length,  $\Delta x$  is the length of the compartment of isopotential membrane and  $I_a$  is the axial current between neighboring compartments. From equation 5.1

$$V_{in} = V_m + V_{out}$$

and since the compartments of the model are small ( $\Delta x \rightarrow 0$ ), then

$$r_i I_a(x, t) = -\frac{\partial V_i(x, t)}{\partial x}$$

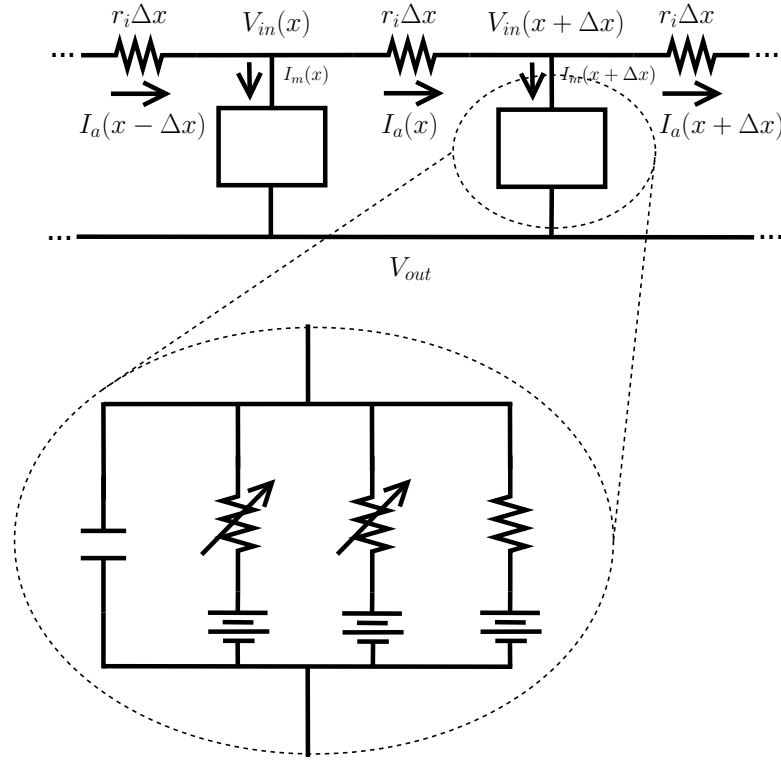


Figure 5.6: Circuit diagram of a non-branched multi-compartment model.

$$r_i I_a(x, t) = - \left( \frac{\partial V_m(x, t)}{\partial x} + \frac{\partial V_{out}(x, t)}{\partial x} \right) \quad (5.5)$$

The axial current  $I_a(x, t)$  between neighboring compartments at a given moment in time is also equal to the axial current flowing through the previous compartments plus the current flow across the cell membrane

$$I_a(x, t) = I_a(x + \Delta x, t) + I_m(x + \Delta x, t)$$

defining  $\hat{i}_m = \frac{I_m}{\Delta x}$

$$I_a(x, t) = I_a(x + \Delta x, t) + \Delta x \hat{i}_m(x + \Delta x, t)$$

isolating  $\hat{i}_m$ , and using once again the fact that  $\Delta x \rightarrow 0$ , then

$$\hat{i}_m(x, t) = - \frac{\partial I_a(x, t)}{\partial x} \quad (5.6)$$

From equations 5.5 and 5.6 it follows that

$$\begin{aligned} -r_i \frac{\partial I_a(x, t)}{\partial x} &= \frac{\partial}{\partial x} \left( \frac{\partial V_m(x, t)}{\partial x} + \frac{\partial V_{out}(x, t)}{\partial x} \right) = r_i \hat{i}_m(x, t) \\ -r_i \frac{\partial I_a(x, t)}{\partial x} &= \frac{\partial^2 V_m(x, t)}{\partial x^2} + \frac{\partial^2 V_{out}(x, t)}{\partial x^2} = r_i \hat{i}_m(x, t) \end{aligned} \quad (5.7)$$

Including the spatial dependences in equation 5.4, the membrane current per unit area  $i_m$  is defined as

$$i_m(x, t) = c_m \frac{\partial V_m(x, t)}{\partial t} + i_{ion}(x, t) \quad (5.8)$$

For a cylindrical compartment of diameter  $d$  and length  $\Delta x$  the current per unit length  $\hat{i}_m$  can be expressed in terms of  $i_m$  as

$$\hat{i}_m = \pi d i_m \quad (5.9)$$

then from equations 5.7, 5.8, and 5.9 we have that

$$\frac{\partial^2 V_m(x, t)}{\partial x^2} + \frac{\partial^2 V_{out}(x, t)}{\partial x^2} = \pi d r_i \left( c_m \frac{\partial V_m(x, t)}{\partial t} + i_{ion}(x, t) \right) \quad (5.10)$$

reorganizing equation 5.10, expressing the second derivative of  $V_m$  with respect to  $x$  as a discrete expression in terms of  $\Delta x$ , and introducing compartment notation, e.g.  $V_m(x, t) = V_m^{(n)}$ ,  $V_m(x + \Delta x, t) = V_m^{(n+1)}$ , we obtain that

$$\begin{aligned} \frac{dV_m^{(n)}}{dt} &= \frac{1}{c_m} \left( \frac{1}{r_i d \pi} (\phi_m + \phi_o) - i_{ion} \right) \\ \phi_m &= \frac{V_m^{(n-1)} - 2V_m^{(n)} + V_m^{(n+1)}}{\Delta x^2} \\ \phi_o &= \frac{V_o^{(n-1)} - 2V_o^{(n)} + V_o^{(n+1)}}{\Delta x^2} \end{aligned} \quad (5.11)$$

where  $V_m^{(n)}$  and  $V_o^{(n)}$  are the transmembrane potential and the extracellular potential at the  $n$ th compartment,  $c_m$  is the specific membrane capacitance,  $r_a$  is the intracellular axial resistance per unit length,  $\Delta x$  and  $d$  are the compartment length and diameter, respectively, and  $i_{ion}$  is the total ionic current flowing through the membrane at a given moment in time [20,22,23]. Equation 5.11 is a description of how the membrane potential changes along a multi-compartment model of a neural fiber in response to external electrical stimulation.

As a final remark for this section, it is worth noting that the level of detail of a multi-compartment model is determined by the number of compartments used to represent the neuron's morphology. A model with a large number of extremely small compartments can provide a highly accurate representation of a neuron's morphology and electrical behavior, but since the number of differential equations of the model is proportional to the number of compartments — equation 5.11 and the associated set of differential equations for  $i_{ion}$  have to be solved for each compartment of the neuron, or set of neurons, of the model — it also translates into increased computational cost.

## 5.2 Emulation of computer models

A computer model is a mathematical abstraction of a physical system implemented as a computer program. A computer model, represented by a function  $y = f(x)$ , allows to study the response of the modeled system to varying inputs, each input corresponding to a specific choice of  $x$ . But computer experiments, evaluating  $f$  at different choices of  $x$ , can be difficult to perform when the computer model is computationally expensive, that is, when calculating  $f(x)$  for a single  $x$  takes too long to compute (when compared

with the time available to perform a particular experiment). Thus arises the need of finding ways to obtain  $y = f(x)$  for  $N$  inputs  $x$ ,  $y_1 = f(x_1), \dots, y_N = f(x_N)$ , given a limited number  $n$  of model runs,  $y_1 = f(x_1), \dots, y_n = f(x_n)$  with  $n < N$ .

An emulator is a statistical representation of a computer model, a probability distribution over  $f$ , that once obtained is used to address the issue under study without additional runs of the original model.

$$p(f(x_{n+1}), \dots, f(x_N) | f(x_1), \dots, f(x_n))$$

The main approach to developing emulators uses Gaussian processes. A Bayesian framework, and Gaussian process regression in particular, allow not only to predict outputs at inputs not previously run, but also to quantify uncertainty in the model outputs induced by uncertainty in the inputs [16, 17]. However, because of its nature, the VTA estimation problem is better described as a classification problem (see section 6.2 for details). Our emulator will therefore be based on a Gaussian process classifier (GPC).

### 5.2.1 Gaussian process classification

A Gaussian process (GP) is defined as a probability distribution over functions  $f(\mathbf{x})$ ,  $\mathbf{x} \in \mathcal{X}$ , such that the values of said functions evaluated at an arbitrary set of points  $\mathbf{X} \subset \mathcal{X}$  jointly have a Gaussian distribution, that is,  $p(\mathbf{f} | \mathbf{X}, \boldsymbol{\theta}) = \mathcal{N}(\mathbf{f} | \mathbf{m}, \mathbf{K})$ . The mean vector  $\mathbf{m}$  and covariance matrix  $\mathbf{K}$  completely specify the GP, and are obtained from associated mean and covariance (kernel) functions,  $m(\mathbf{x})$  and  $k(\mathbf{x}, \mathbf{x}')$  respectively, that may additionally depend on a set of hyperparameters  $\boldsymbol{\theta}$  [24].

Gaussian process usually are used as prior distributions over a function space. The uncertainty over the function space is updated using a set of observations and Bayesian inference. Bayesian inference is a method of statistical inference that introduces a hypothesis, a prior distribution, before observing any data from the system under analysis, and then uses Bayes theorem to compute a posterior probability distribution given the observed data, that is the uncertainty in the hypothesis after the data is observed.

In general, the idea behind binary GP classification works as follows: given a set of inputs  $\mathbf{X} = [\mathbf{x}_1, \dots, \mathbf{x}_n]^T$  and their associated labels  $\mathbf{y} = [y_1, \dots, y_n]^T$ , with  $y_i \in \{-1, 1\}$ , the probability  $p(y | \mathbf{x})$  is represented by the latent function that describes the data  $f(\mathbf{x})$  mapped to the unit interval through a sigmoid function  $\sigma$ . If  $\sigma$  is symmetric then  $p(y | \mathbf{x}) = \sigma(y f(\mathbf{x}))$ , and the joint likelihood  $p(\mathbf{y} | \mathbf{f})$ , where  $\mathbf{f} = [f_1, \dots, f_n]^T$  with  $f_i = f(\mathbf{x}_i)$ , can be expressed as

$$p(\mathbf{y} | \mathbf{f}) = \prod_{i=1}^n \sigma(y_i f(\mathbf{x}_i)) \quad (5.12)$$

Imposing a Gaussian prior over  $\mathbf{f}$ , and assuming a zero mean function,  $p(\mathbf{f} | \mathbf{X}, \boldsymbol{\theta}) = \mathcal{N}(\mathbf{f} | \mathbf{0}, \mathbf{K})$ , the posterior probability becomes

$$\begin{aligned} p(\mathbf{f} | \mathcal{D}, \boldsymbol{\theta}) &= \frac{p(\mathbf{y} | \mathbf{f}) p(\mathbf{f} | \mathbf{X}, \boldsymbol{\theta})}{p(\mathcal{D} | \boldsymbol{\theta})} \\ &= \frac{\mathcal{N}(\mathbf{f} | \mathbf{0}, \mathbf{K})}{p(\mathcal{D} | \boldsymbol{\theta})} \prod_{i=1}^n \sigma(y_i f(\mathbf{x}_i)) \end{aligned}$$

where  $\mathcal{D} = \{(\mathbf{x}_i, y_i) | i = 1, \dots, n\}$  is the observed data. Then, the class probabilities for a new data pair  $(\mathbf{x}_*, y_*)$  can be obtained marginalizing  $\mathbf{f}$

$$p(f_*|\mathcal{D}, \boldsymbol{\theta}, \mathbf{x}_*) = \int p(f_*|\mathbf{f}, \mathbf{X}, \boldsymbol{\theta}, \mathbf{x}_*)p(\mathbf{f}|\mathcal{D}, \boldsymbol{\theta})d\mathbf{f}$$

and computing the expectation

$$\begin{aligned} p(y_*|\mathcal{D}, \boldsymbol{\theta}, \mathbf{x}_*) &= \int p(y_*|f_*)p(f_*|\mathcal{D}, \boldsymbol{\theta}, \mathbf{x}_*)df_* \\ &= \int \sigma(y_*f(\mathbf{x}_*))p(f_*|\mathcal{D}, \boldsymbol{\theta}, \mathbf{x}_*)df_* \end{aligned}$$

In a Bayesian framework GPs offer the advantage of analytical tractability: a Gaussian prior (the assumption made before observing the data) and a Gaussian likelihood (how probable the data set is given the assumption) will result in a Gaussian posterior (the uncertainty in the assumption after the data is observed), and even though the discrete nature of the classification problem gives rise to a non-Gaussian likelihood (Eq. 5.12) a posterior distribution can still be approximated by methods such as Lapace approximation or Expectation Propagation.

Laplace's method approximates the posterior doing a second order Taylor expansion of  $\log p(\mathbf{f}|\mathcal{D}, \boldsymbol{\theta})$  around the maximum of the unnormalized posterior  $p(\mathbf{y}|\mathbf{f})p(\mathbf{f}|\mathbf{X}, \boldsymbol{\theta})$ ,

$$p(\mathbf{f}|\mathcal{D}, \boldsymbol{\theta}) \approx \mathcal{N}(\mathbf{f}|\hat{\mathbf{f}}, \mathbf{A}^{-1}) \propto \exp\left(-\frac{1}{2}(\mathbf{f} - \hat{\mathbf{f}})^T \mathbf{A}(\mathbf{f} - \hat{\mathbf{f}})\right)$$

where  $\hat{\mathbf{f}} = \underset{\mathbf{f}}{\operatorname{argmax}} p(\mathbf{y}|\mathbf{f})p(\mathbf{f}|\mathbf{X}, \boldsymbol{\theta})$  and  $\mathbf{A} = -\nabla\nabla\log p(\mathbf{f}|\mathcal{D}, \boldsymbol{\theta})|_{\mathbf{f}=\hat{\mathbf{f}}}$ . The hyperparameters  $\boldsymbol{\theta}$  of the covariance function are selected so that they maximize the evidence or marginal likelihood  $p(\mathcal{D}|\boldsymbol{\theta})$ . From the results of Laplace's method the logarithm of this quantity can be approximated as

$$\log p(\mathcal{D}|\boldsymbol{\theta}) \simeq \log p(\hat{\mathbf{f}}|\mathcal{D}, \boldsymbol{\theta}) + \frac{n}{2}\log(2\pi) + \frac{1}{2}\log|\mathbf{A}^{-1}|$$

For details about Gaussian process classification see [25, 26, 27].

---

## 6. Materials and methods

---

### 6.1 Gold standard for VTA estimation

The gold standard for VTA estimation, schematized in Figure 6.1, aims to model the response of the brain tissue to the electrical stimulation delivered by the DBS electrode. To that end, the electric potential generated by the DBS electrode is coupled to a model of multi-compartment axons arranged in a field around the electrode shaft. Axons that because of the stimulation fire action potentials in a one to one ratio with the DBS pulses are considered active, and their spatial distribution defines the VTA.

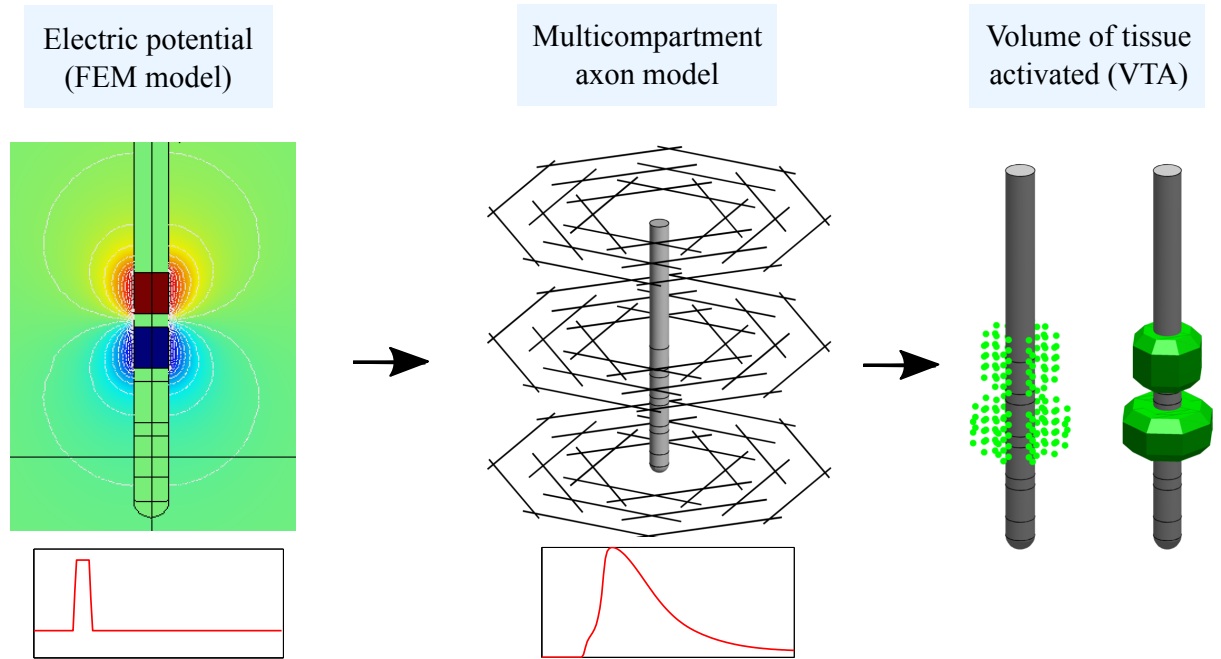


Figure 6.1: Gold standard for VTA estimation. The electric potential, previously computed by means of, for example, the finite element method (FEM) [28], is interpolated onto each section of a field of multi-compartment axons. They represent the brain tissue surrounding the DBS electrode. The response of the axons to the stimulation defines the volume of tissue activated: axons that fire an action potential per stimulation pulse are considered active and their positions in space give form to the VTA.

### 6.1.1 Electric potential propagation in the brain tissue

In this work the calculation of the electric potential generated by the DBS electrode was carried out in the finite element method (FEM) software COMSOL Multiphysics 4.2. A simplified 3D model of a clinical electrode (Medtronic DBS 3389 electrode) positioned in the middle of a conductive extracellular medium was built. The simplified electrode model consisted of four conductive contacts ( $4 \times 10^6 \text{ Sm}^{-1}$ ) 1.27 mm in width and 1.5 mm in height separated by insulating bands ( $1 \times 10^{-10} \text{ Sm}^{-1}$ ) 0.5 mm in height, and of an insulating semicircular tip with radius 0.635 mm (Figure 6.2a) [29]. The brain tissue was modeled as a sphere of diameter 10 cm. First, a bulk tissue conductivity of  $0.3 \text{ Sm}^{-1}$  was used to account for the isotropic assumption. Then diffusion tensor based conductivities were used to represent the tissue anisotropy of the basal ganglia region. The diffusion tensors were estimated from the DTI30 dataset<sup>1</sup>, with the RESTORE (Robust Estimation of Tensors by Outlier Rejection) algorithm [30], and then linearly transformed to conductivity tensors [31]. In both cases a representation of a 0.5 mm encapsulation layer around the electrode was also included, and its conductivity was set to three different values ( $0.680 \text{ Sm}^{-1}$ ,  $0.128 \text{ Sm}^{-1}$ ,  $0.066 \text{ Sm}^{-1}$ ) to represent low ( $\sim 500 \Omega$ ), medium ( $\sim 1000 \Omega$ ), and high ( $\sim 1500 \Omega$ ) impedance conditions [13, 32]. The model also integrated the voltage drop at the electrode-tissue interface. The boundary conditions used were the same as in [7] and [15]. The stimulation was modeled by imposing Dirichlet boundary conditions on the active contacts of the electrode. Dirichlet boundary conditions were also used to ground the boundaries of the extracellular medium. Zero current flow conditions were imposed on the surfaces of the inactive contacts and insulating components of the electrode. Finally, Poisson's equation was solved to obtain the voltage propagation in the brain tissue.

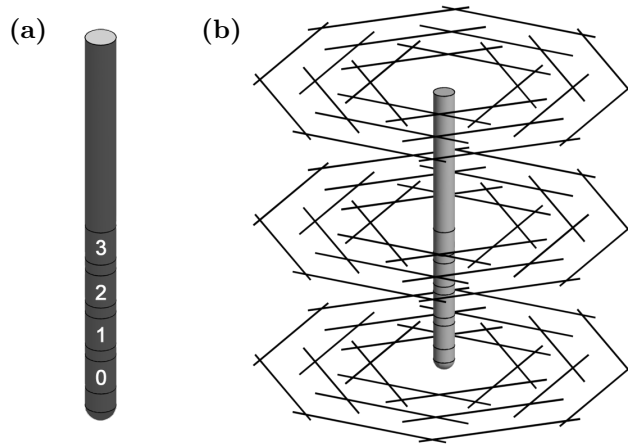


Figure 6.2: **(a)** DBS electrode model. The electrode contacts were numbered from 0 to 3. **(b)** Orientation of the axons around the electrode shaft (for visualization purposes only a small fraction of the total axonal population is shown).

### 6.1.2 Axonal distribution and VTA estimation

In the VTA modeling literature, multicompartment neuron models are often restricted to axonal models, since axons have been shown to drive the basic neural response to external electrical stimulation. In addition to this behaviour, the fundamental biophysics of how axonal response to external electrical stimulation

<sup>1</sup> Available at [www.cabiatl.com/CABI/resources/dti-analysis/](http://www.cabiatl.com/CABI/resources/dti-analysis/)

works is independent of neuron type [33, 34, 35]. The axonal model used in this work corresponds to the multicompartment myelinated axon model detailed in [11]. Briefly, each axon includes 21 nodes of Ranvier, 2 myelin attachment segments, 2 paranode main segments, and 3 internode segments between each node. The nodes are modeled by a parallel combination of the membrane capacitance with nonlinear conductances (fast  $\text{Na}^+$ , persistent  $\text{Na}^+$ , and slow  $\text{K}^+$ ) and a linear leakage conductance. The paranodal and internodal compartments include two concentric layers, each including a linear conductance in parallel with the membrane capacitance, to represent the myelin sheath and the axolemma. Equations 6.1 to 6.5 describe the ionic currents at the nodes of Ranvier, and whose dynamics are ultimately responsible for the occurrence of an action potential, and therefore of activation at a given node:

$$i_{ion} = i_{Naf} + i_{Nap} + i_{Ks} + i_{LK} \quad (6.1)$$

$$i_{Naf} = g_{Naf} m^3 h (V_m - E_{Na}) \quad (6.2)$$

$$i_{Nap} = g_{Nap} p^3 (V_m - E_{Na}) \quad (6.3)$$

$$i_{Ks} = g_{Ks} s (V_m - E_K) \quad (6.4)$$

$$i_{LK} = g_{LK} (V_m - E_{LK}) \quad (6.5)$$

The values of the gating variables  $m$ ,  $h$ ,  $p$ , and  $s$ , are computed at each time step from equations 6.6 to 6.17. Tables 6.1 and 6.2 show the values of the morphological and electrical parameters used in the myelinated axon model, respectively.

$$\frac{dm}{dt} = \alpha_m (1 - m) - \beta_m m \quad (6.6)$$

$$\alpha_m = \frac{6.57(V_m + 20.4)}{1 - \exp[-(V_m + 20.4)/10.3]} \quad (6.7)$$

$$\beta_m = \frac{0.304[-(V_m + 25.7)]}{1 - \exp[(V_m + 25.7)/9.16]} \quad (6.8)$$

$$\frac{dh}{dt} = \alpha_h (1 - h) - \beta_h h \quad (6.9)$$

$$\alpha_h = \frac{0.34[-(V_m + 114)]}{1 - \exp[(V_m + 114)/11]} \quad (6.10)$$

$$\beta_h = \frac{12.6}{1 - \exp[-(V_m + 31.8)/13.4]} \quad (6.11)$$

$$\frac{dp}{dt} = \alpha_p (1 - p) - \beta_p p \quad (6.12)$$

$$\alpha_p = \frac{0.0353(V_m + 27)}{1 - \exp[-(V_m + 27)/10.2]} \quad (6.13)$$

$$\beta_p = \frac{0.000883[-(V_m + 34)]}{1 - \exp[(V_m + 34)/10]} \quad (6.14)$$

$$\frac{ds}{dt} = \alpha_s (1 - s) - \beta_s s \quad (6.15)$$

$$\alpha_s = \frac{0.3}{1 - \exp[(V_m + 53)/(-5)]} \quad (6.16)$$

$$\beta_s = \frac{0.03}{1 - \exp[(V_m + 90)/(-1)]} \quad (6.17)$$

To estimate the volume of tissue activated a population of 8112 straight axons of diameter  $5.7 \mu\text{m}$  was built around the electrode shaft. The axonal fibers were oriented in four different directions, perpendicular to the axis of the electrode (Figure 6.2b), and with a distance between axons of  $0.5 \text{ mm}$  in both the vertical and horizontal directions. This axonal distribution aimed to capture the spatial spread of activation in response to the stimulus in several directions around the electrode, considering that under anisotropic conductivity conditions the electric potential would change as a function of the direction of propagation [36].

Parameter	Value ( $\mu\text{m}$ )
Fiber diameter	5.7
Node-node separation	500
Number of myelin lemmella	80
Nodo length	1
Node diameter	1.9
MYSA length	3
MYSA diameter	1.9
MYSA periaxonal space width	0.002
FLUT length	35
FLUT diameter	3.4
FLUT periaxonal space width	0.004
STIN length	70.5
STIN diameter	3.4
STIN periaxonal space width	0.004

Table 6.1: Morphological parameters of the multi-compartment myelinated axon model [11]

To simulate the neurostimulation the values of the electric potential were linearly interpolated from the nodes of the FEM solution onto each of the axonal model compartments. An axon was considered active if it fired in a one to one ratio with a DBS stimulation pulse. The VTA was defined as the volume enclosed by the locations of the central nodes of Ranvier of the activated axons [36]. The simulations of the axonal response to the electric stimulation, based on the solution of equation 5.11, were implemented in NEURON 7.3<sup>2</sup> configured as a Python module [37]. NEURON is a widely used tool to simulate the electrical behaviour of biological neurons [38]. Its compatibility with Python allowed us to implement most of the VTA estimation model without the hurdles of changing programming platforms.

A full implementation of the gold standard for VTA estimation was used first to study the effects of the stimulation parameters on the VTA and then to compute volumes of tissue activated, for several combinations of stimulation parameter settings (see Table 6.3), that would serve as reference data sets to evaluate the performance of the proposed emulator.

<sup>2</sup>[www.neuron.yale.edu/neuron/download](http://www.neuron.yale.edu/neuron/download)

Parameter	Value	Unit
Nodal capacitance ( $c_n$ )	2	
Internodal capacitance ( $c_i$ )	2	$\frac{\mu F}{cm^2}$
Myelin capacitance ( $c_m$ )	0.1	
Axoplasmic resistivity ( $\rho_a$ )	70	$\Omega cm$
Periaxonal resistivity ( $\rho_p$ )	70	
Myelin conductance ( $g_m$ )	0.001	
MYSa conductance ( $g_a$ )	0.001	
FLUT conductance ( $g_f$ )	0.0001	
STIN conductance ( $g_i$ )	0.0001	$\frac{S}{cm^2}$
Maximum fast $Na^+$ conductance ( $g_{Na_f}$ )	3.0	
Maximum slow $K^+$ conductance ( $g_{K_s}$ )	0.08	
Maximum persistent $Na^+$ conductance ( $g_{Na_p}$ )	0.01	
Nodal leakage conductance ( $g_{LK}$ )	0.007	
$Na^+$ Nernst potential ( $E_{Na}$ )	50.0	$mV$
$K^+$ Nernst potential ( $E_K$ )	-90.0	
Leakage reversal potential ( $E_{LK}$ )	-90.0	
Rest potential ( $V_{rest}$ )	-80.0	

Table 6.2: Electrical parameters of the multi-compartment myelinated axon model [11]

Monopolar		
	Base parameters	Variation range
Active contacts	3	3
Amplitude	-3 V	-1, -2, -3, -4, -5 V
Pulse-width	90 $\mu s$	60, 90, 210, 450 $\mu s$
Impedance	900 $\Omega$	500, 900, 1500 $\Omega$
Bipolar {-}		
	Base parameters	Variation range
Active contacts	2, 3	2, 3
Amplitude	-3 V	-1, -2, -3, -4, -5 V
Pulse-width	90 $\mu s$	60, 90, 210, 450 $\mu s$
Impedance	900 $\Omega$	500, 900, 1500 $\Omega$
Bipolar { $\pm$ }		
	Base parameters	Variation range
Active contacts	2, 3	2, 3
Amplitude	$\pm 3$ V	$\pm 1, \pm 2, \pm 3, \pm 4, \pm 5$ V
Pulse-width	90 $\mu s$	60, 90, 210, 450 $\mu s$
Impedance	900 $\Omega$	500, 900, 1500 $\Omega$

Table 6.3: Realistic stimulation parameter settings used in this study (Medtronic ACTIVA-RC stimulator). The base parameters were varied, one at a time, in a range of possible values for the three active contact configurations considered: one cathode (monopolar), cathode-cathode (bipolar {-}), and anode-cathode (bipolar { $\pm$ }). Every set of stimulation parameters and encapsulation tissue impedances was used under both isotropic and anisotropic conductivity conditions.

## 6.2 Gaussian process emulation of the VTA

Active axons, whose distribution defines the VTA, fire one action potential for each stimulation pulse delivered by the stimulator. Inactive axons fail to respond in such a way. It follows that active and inactive axons can be thought of as part of two different classes. Additionally, all axons are independent from one another. Their response to the stimulation depends only on the electric potential along their lengths. Thus, determining the volume of tissue activated from a field of axons is equivalent to a binary classification problem: Whether an individual axon is active can be thought of as the outcome of a binary function  $f(\mathbf{x})$ , where  $\mathbf{x}$  is an input vector that contains information about the axon's spatial location and the electric potential at that location. The VTA can then be obtained evaluating  $f$  multiple times for an appropriate set of  $N$  input vectors  $\mathbf{x}$ . Under this premise, an emulator can be used to accelerate the estimation of the VTA by computing the response to the stimulation of  $n$  axons ( $n < N$ ) and then using that information to predict the behaviour of an axonal population large enough to represent accurately the region of interest around the electrode shaft. This approach is summarized in Figure 6.3

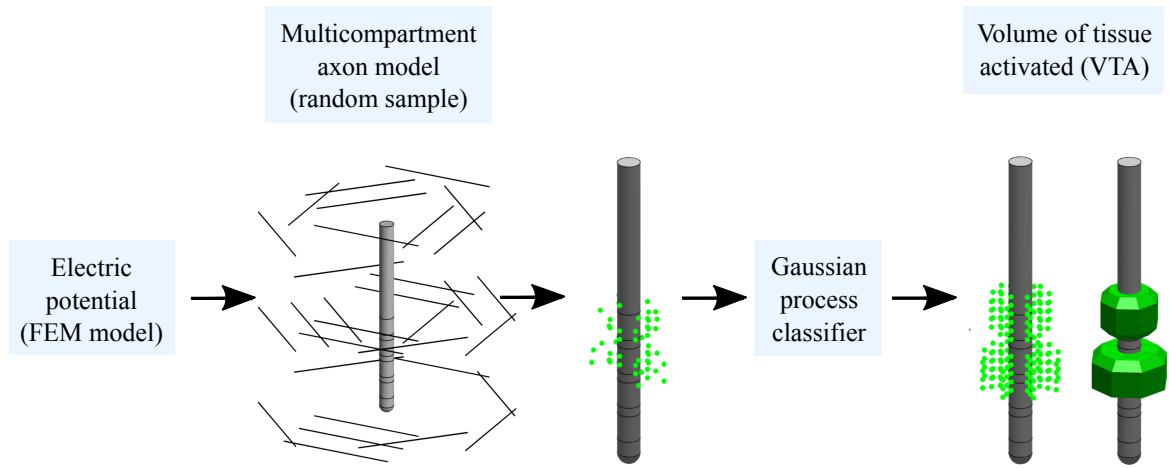


Figure 6.3: A small random sample of axons is taken from an axonal population, built as detailed in section 6.1.2. With this reduced model a multi-compartment model simulation is executed in order to obtain labeled data to train a GP classifier. Then, the classifier is used to predict which elements of the entire axonal population would be active, obtaining an estimation of the VTA.

### 6.2.1 Implementation

A random sample of  $n = 500$  axons was taken from a total axonal population of 8112 axons, built as detailed in section 6.1.2. The axons were sampled from a uniform distribution with respect to the euclidean distance between their central nodes of Ranvier and the center of the active contact. When more than one contact was active the above procedure was repeated, sampling, for each of them, a number of axons equal to  $n$  divided by the number of active contacts. Next, a multicompartment simulation was executed to determine which of the sampled neural fibers were active during the stimulation. The information provided by the multicompartment simulation was converted to a set of labeled data  $\{(\mathbf{x}_i, y_i) | i = 1, \dots, n\}$ , where  $\mathbf{x}_i = [x_{i1}, x_{i2}, x_{i3}]$  is a vector of characteristics for each axon or data point, and  $y_i$  is its corresponding label (active: 1, inactive: -1). This data were used to train a Gaussian process-based classifier. All inputs to

the classification algorithm (pyGPs library<sup>3</sup> for Python 2.7) are depicted in Figure 6.4; they were selected so that the relationship between activation, the position of each axon with respect to the electrode shaft, and the electric potential was represented in the classification outcome.

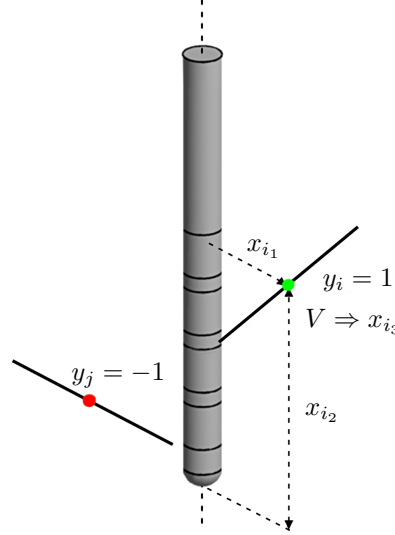


Figure 6.4: Inputs to the classification algorithm.  $x_{i1}$ : distance between the central nodes of Ranvier and the axis of the DBS electrode.  $x_{i2}$ : distance between the central nodes of Ranvier and the plane containing the electrode tip and that is perpendicular to the electrode axis.  $x_{i3}$ : value of the electric potential ( $V$ ) at each central node of Ranvier.  $y$ : label that identified the axons as being either active (1) or inactive (-1).

The classifier was trained with 70% of the data obtained from the multicompartment axon model, assuming a logistic likelihood function ( $\sigma$ ), prescribing a general purpose kernel (squared exponential covariance function with automatic relevance determination), and using Laplace's approximation to the posterior. The hyperparameters of the kernel were selected minimizing the Laplace approximation of the negative log marginal likelihood. The inference method was chosen due to computational cost considerations [27].

Since a GP classifier assigns class probabilities instead of labels (Figure 6.5), a cut off probability was determined with a receiver-operating characteristic (ROC) analysis performed on all available data from the multicompartment model (Figure 6.6). Then the VTA was estimated by predicting which of the 8112 central nodes of Ranvier of the entire axonal population, and therefore the axonal fibers they belong to, would be activated by the applied stimulus.

Finally, the spreads of activation predicted by the classifier, in 30 independent simulation runs, for each of the stimulation parameters shown in Table 6.3 were compared against those obtained with activation threshold curves customized to our data [12, 15], in terms of the prediction error

$$error = \frac{FP + FN}{AA}$$

<sup>3</sup>[github.com/marionmari/pyGPs](https://github.com/marionmari/pyGPs)

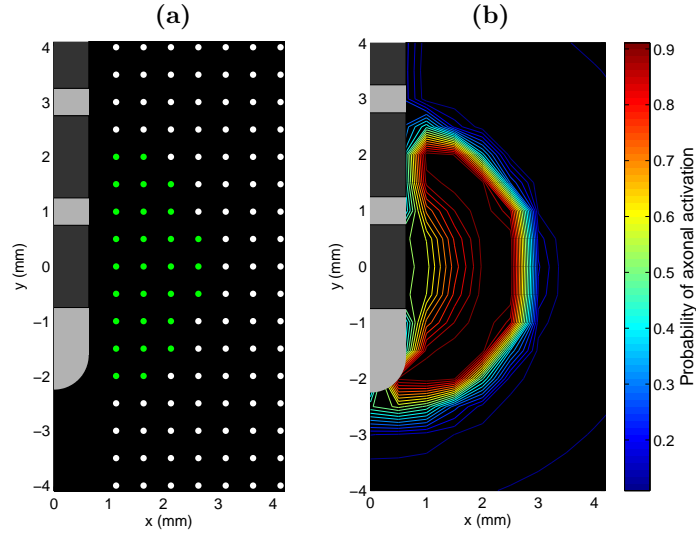


Figure 6.5: **(a)** Lateral view of a full axonal field. Active and inactive axons are depicted as green and white dots, respectively. **(b)** Class probabilities assigned by the GP classifier. Higher probabilities are assigned to the regions where the active axons predominate.

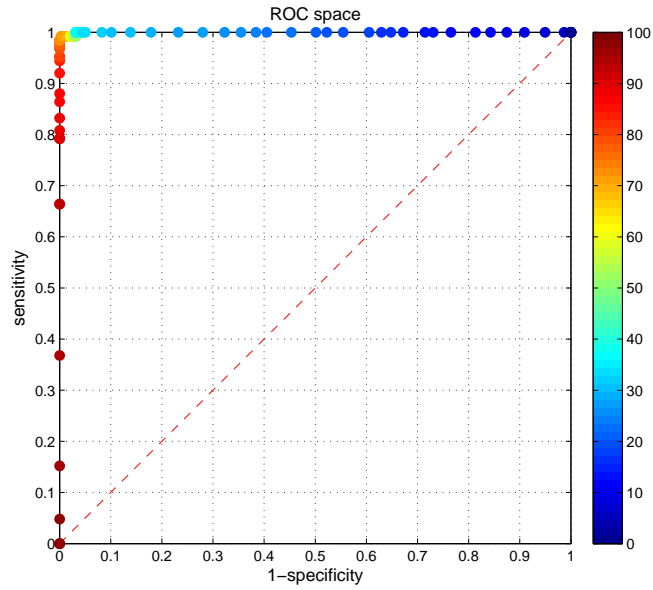


Figure 6.6: Plot of an instance of the ROC analysis used to determine the probability threshold above which axons were considered active. The threshold was chosen so that it generated the closest value, in the sense of the euclidean norm, to the ideal classification point (0,1). The sensitivity and 1-specificity values correspond to the true-positive rate, and to the false-positive rate, respectively. The color map represents different probability values.

where  $FP$  and  $FN$  are the false positives and false negatives with respect to the reference data set, and  $AA$  is the reference number of active axons.

---

## 7. Results and discussion

---

### 7.1 Effects of the stimulation parameters on the VTA

In this section we make a parenthesis to analyse the changes in the VTA during deep brain stimulation as a function of the stimulation parameters. The aim of this analysis is twofold. First, to justify why unlike the amplitude and the pulse width the frequency of stimulation was not included as one of the parameters varied to evaluate the performance of the our emulator (Table 6.3). This despite the fact that the frequency of stimulation is critical in the outcome of DBS [5,6]. And second to clarify the extent to which the VTA can represent the effects of DBS in cerebral activity. The simulations in this section were carried out using the gold standard for VTA estimation, activating contact number 3 only (see figure 6.2a), assuming an isotropic conductivity for the extracellular medium and an encapsulation tissue impedance of  $1000\ \Omega$ .

#### Amplitude and pulse width

To study the effect of stimulation amplitude variation on the VTA we fixed the pulse width to  $90\ \mu\text{s}$ , and set the stimulation amplitude to  $-1\ \text{V}$ ,  $-2\ \text{V}$ , and  $-3\ \text{V}$ . The results are shown in Figure 7.1. To study the effect of pulse width on the VTA we fixed the stimulation amplitude to  $-3\ \text{V}$ , and set the pulse width to  $60\ \mu\text{s}$ ,  $90\ \mu\text{s}$ , and  $450\ \mu\text{s}$ . The results are shown in Figure 7.2.

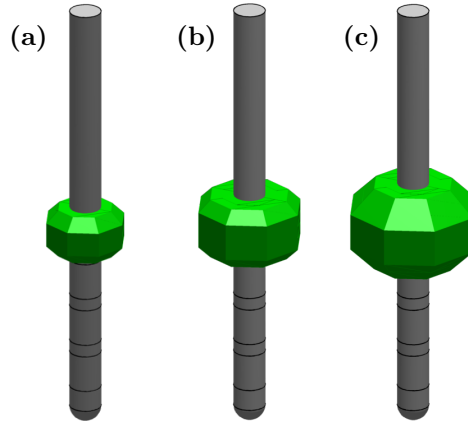


Figure 7.1: Volumes of tissue activated for three different stimulation amplitudes: (a)  $1\ \text{V}$ , (b)  $2\ \text{V}$ , (c)  $3\ \text{V}$  (cathodic,  $90\ \mu\text{s}$  stimulation pulses).

Figures 7.1 and 7.2 clearly show that the volume of tissue activated grows as the amplitude of stimulation and the pulse width increase. These results are in agreement with previous studies about the variation of the VTA due to changes in the pulse width and amplitude of stimulation [3], and can be understood in

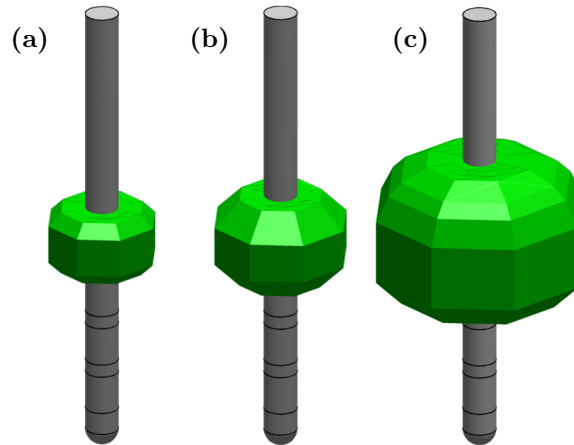


Figure 7.2: Volumes of tissue activated for three different pulse widths: **(a)**  $60 \mu\text{s}$ , **(b)**  $90 \mu\text{s}$ , **(c)**  $250 \mu\text{s}$  (cathodic, 3 V stimulation pulses).

a straightforward fashion from basic neural activation theory. Larger stimulation amplitude means larger electric potential values (an larger values of its second order spatial difference) at longer distances from the active contact of the electrode, axons at locations where the stimulation is sub-threshold for a given amplitude could experience supra-threshold stimulus for larger amplitudes. In a similar manner, a larger pulse width means that axons are stimulated for a longer period of time, and thus, axons at locations where the stimulation amplitude alone is not enough to evoke an action potential would fire because they are being stimulated for longer. Figures 7.3 and 7.4 exemplify this kind of behavior in one myelinated axon stimulated with an intracellular injection of current.

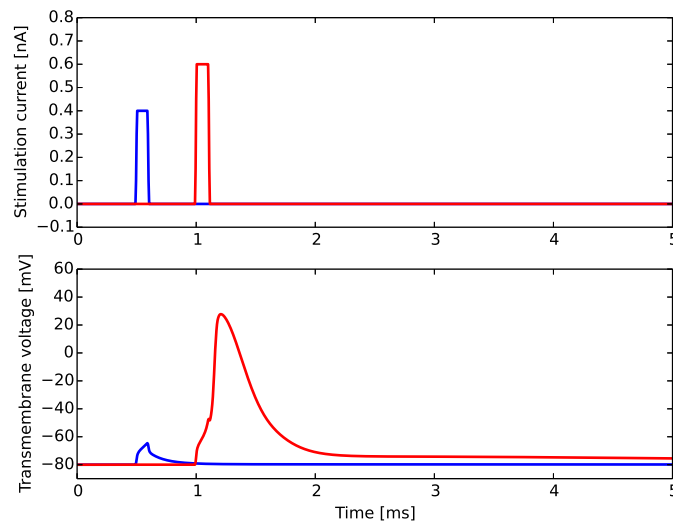


Figure 7.3: An increase in the amplitude of the stimulus can easily change the response of the neural fiber from sub-threshold (blue) to supra-threshold (red).

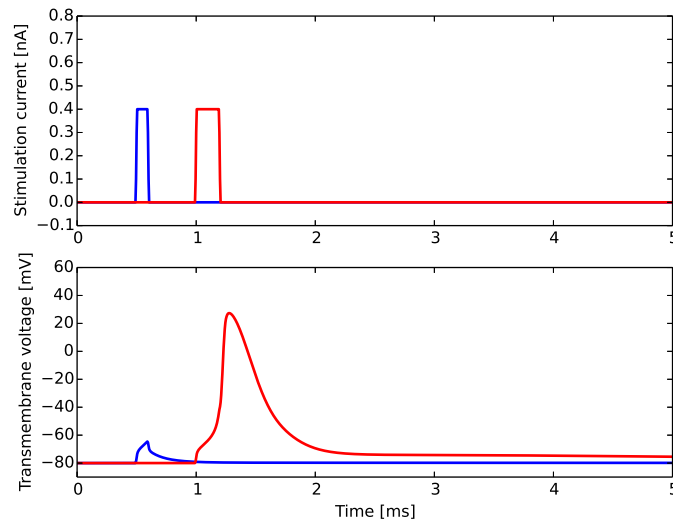


Figure 7.4: An increase in the duration of the stimulus can also change the response of the neural fiber from sub-threshold (blue) to supra-threshold (red), even for stimuli of the same amplitude.

### Frequency

To study the effects of stimulation frequency variation on the VTA we fixed the stimulation amplitude to -3 V, the pulse width to 90  $\mu$ s, and set the DBS frequency to 70 Hz, 130 Hz, 190 Hz. The results are provided in Figure 7.5. They indicate that the VTA is independent of the frequency of stimulation.

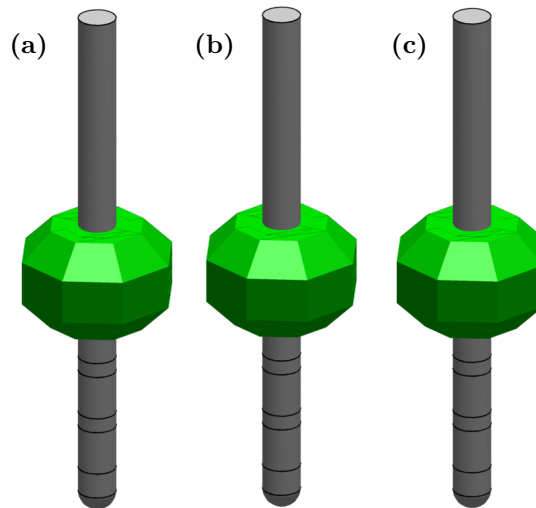


Figure 7.5: Volumes of tissue activated for three different stimulation frequencies: (a) 70 Hz, (b) 130 Hz, (c) 190 Hz (cathodic, 3 V, 90  $\mu$ s stimulation pulses). The volume of tissue activated is a frequency independent metric, at least in the frequency range available in deep brain stimulation devices (2 Hz to 250 Hz).

These findings may seem counter intuitive, since it is a well known fact that the therapeutic results of DBS

depend heavily on the frequency of stimulation [5, 6], yet they are in agreement with previous studies [4]. It is important to note, however, that even though the VTAs at different frequencies are the same, the neural activity taking place in those volumes of tissue does depend on the frequency of stimulation.

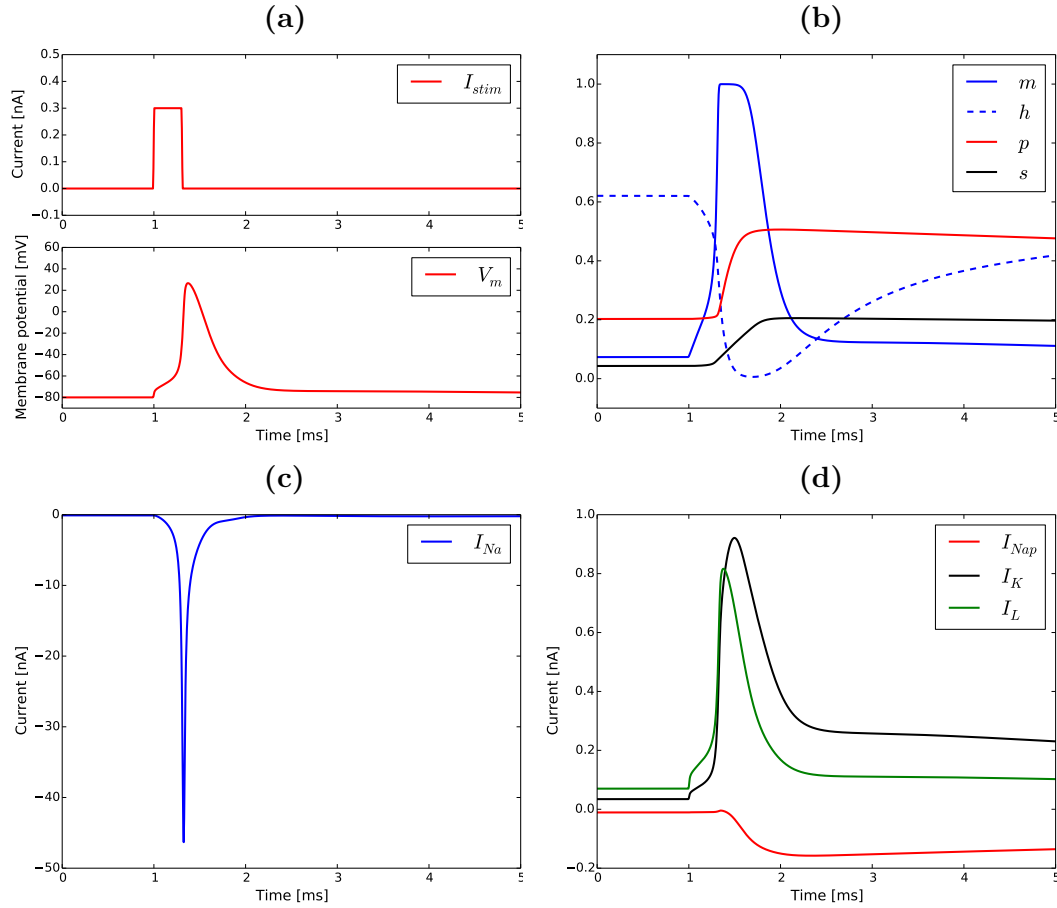


Figure 7.6: In the myelinated axon model [11] the firing of an action potential **(a)** is triggered by a rapid opening of sodium channels, represented by a steep increase in the value of the gating variable  $m$  **(b)**, and by the subsequent influx of sodium ions. However, this abrupt change in the fast sodium current  $i_{Na,f}$  **(c)** is short-lived when compared with the dynamics of the other, slower and smaller currents of the model **(d)**.

The invariance of the VTA with respect to the stimulation frequency can also be explained from basic neural activation theory. Continuous sub-threshold stimulation pulses can produce an action potential, but only if their frequency is high enough to build upon changes in the membrane caused by the previous pulses, that is, if the next pulse happens before the membrane falls back to a state close to rest. In the case of the myelinated axon model, the firing of an action potential (Figure 7.6a) is triggered by a rapid opening of sodium channels, represented by a steep increase in the value of the state or gating variable  $m$  (Figure 7.6b), and by the subsequent influx of sodium ions. However, this abrupt change in the fast sodium current  $i_{Na,f}$  (Figure 7.6c) is short-lived when compared with the dynamics of the other, slower and smaller currents of the model (Figure 7.6d). This is due to the inactivation of sodium channels when the membrane potential reaches a

depolarization threshold. In the axon model this behaviour is represented by a second gating variable,  $h$ , in equation 6.2, that rapidly falls to zero as soon as the membrane potential reaches that threshold, shutting off the fast sodium current  $i_{Na_f}$ . If a stimulation pulse is not large enough to elicit a full fast sodium current response, the next one has to come before the current  $i_{Na_f}$  gets completely back to its resting value, otherwise no action potential will be fired. The second pulse has to be applied in the time window between the opening and inactivation of sodium channels.

In Figure 7.7 we show how sub-threshold intracellular current stimulation pulses of 250 Hz (the maximum frequency of the Medtronic ACTIVA-RC stimulator) are too slow (blue curves) to match the dynamics of  $i_{Na_f}$ . To generate an action potential with sub-threshold stimulus by increasing the frequency, it would have to reach values in the order of kHz (red curves). It follows that in order to increase the volume of tissue activated, or more precisely the spread of direct neural activation (the definition of the VTA doesn't consider action potentials generated by more than one stimulation pulse), varying the frequency alone, this parameter would have to reach a much higher value than what is possible with DBS stimulators. Figure 7.8 shows the spread of neural activation, at 250 Hz and 4 kHz. The spread of neural activation effectively grows at such a high stimulation frequency, but frequencies of the order of kHz are well outside the frequency range that has been shown to be therapeutically beneficial in the treatment of Parkinson's disease (100 Hz - 200 Hz) [5,39].

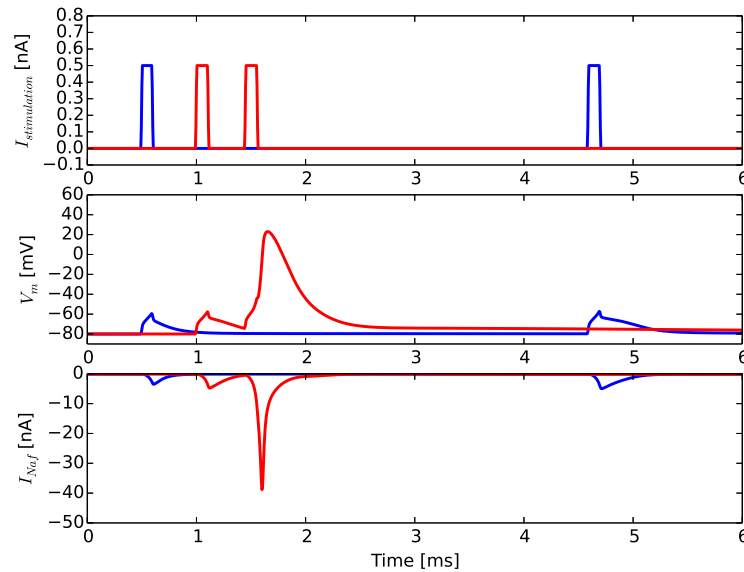


Figure 7.7: Continuous sub-threshold stimulation pulses can produce an action potential, but only if their frequency is high enough (red). The maximum frequency of 250 Hz reached by the DBS stimulator is too low for that purpose (blue).

The volume of tissue activated provides information about which cerebral structures are being directly affected by DBS, but it gives little or no information about how the networks those structures belong to are responding to the stimulation. And it's through the network response that the effects of the frequency of stimulation can be explained. Very briefly, the changes observed in neural activity in subjects with Parkinson's disease include not only increases and decreases of the rate of activity in specific nuclei of the basal ganglia, but also changes in its patterns of activity. These changes occur in the form of increased presence

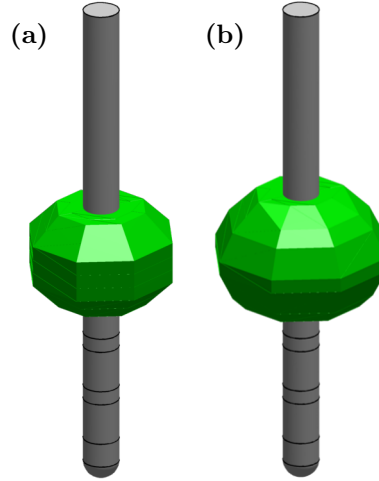


Figure 7.8: Spreads of neural activation for two different stimulation frequencies: **(a)** 250 Hz, the maximum frequency of the Medtronic ACTIVA-RC stimulator, and **(b)** 4 kHz.

of bursts and oscillations, and of synchronization among previously independent nuclei. Stimulation at therapeutically beneficial frequencies replaces those pathologic activity patterns with regular firing that, while not normal, is less deleterious for the basal ganglia-thalamic network function [39, 40].

The VTA can be linked only indirectly to this hypothesis about the mechanisms of action of DBS. Computational models have shown that to achieve a positive therapeutic outcome a large enough number of neural elements must respond to stimulation of an appropriate frequency [5]. The VTA represents a volume such that every neural fiber that goes through it fires action potentials at the stimulation frequency. The larger the VTA, the larger the number of fibers of passage, and of afferent and efferent axons that are propagating neural activity at the stimulation frequency to downstream nuclei. In that sense, a VTA of a large enough size is necessary for DBS to be successful. A smaller VTA would mean that not enough neural elements are responding to the stimulation to mask intrinsic pathological activity.

## 7.2 Evaluation of the performance of the Gaussian process emulator for VTA estimation

In this work we explored a variation to the standard approach to VTA estimation: the VTA is defined by the axons activated for a given set of stimulation parameters (see Figure 7.9). These axons constitute a subset of the axonal field that satisfies certain conditions that differentiate its elements from the rest of the axonal population; active and inactive axons can be viewed as belonging to two different classes.

Based on this premise we aimed to develop a classification system that could reduce the computation time required for VTA estimation, without the shortcomings of alternative methods like activation threshold curves. Namely, the large errors they produce when compared with the gold standard, and their inability to estimate the VTA for multi-contact stimulation. Figure 7.10 summarizes our approach. Instead of a large model with enough axons to describe accurately the region of interest around the electrode shaft, we sampled a comparatively small number of axons from the total axonal population, and with this reduced model we executed a full multicompartment model simulation in order to obtain labeled data to train a GP classifier. Then, we

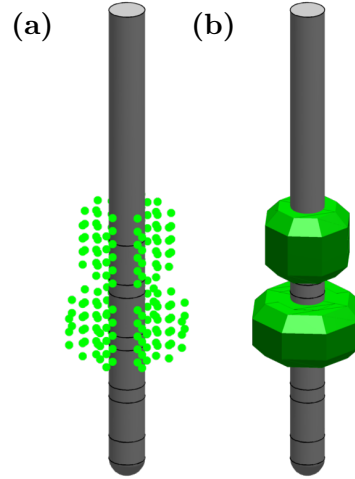


Figure 7.9: **(a)** Locations of the central nodes of Ranvier (dots) of the axons activated by a bipolar (cathode-anode) 3 V, 90  $\mu$ s stimulation pulse, with an encapsulation tissue impedance of 1000  $\Omega$ , and assuming isotropic conductivity conditions. **(b)** The VTA is the volume defined by the spatial distribution of the active axons.

used the classifier to predict which elements of the entire axonal population would be active, obtaining an estimation of the VTA.

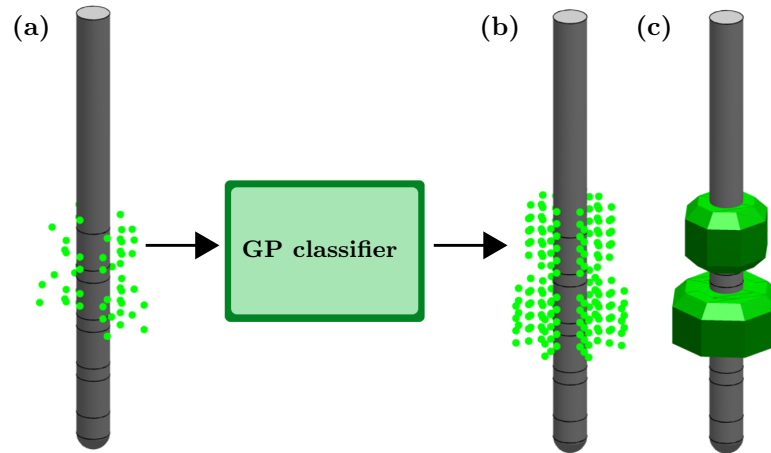


Figure 7.10: **(a)** A multicompartiment model simulation is executed to determine which of the sampled axons are activated by the stimulation (only the locations of active axons are shown). **(b)** The GP classifier uses the labels that identify the sampled axons as either active or inactive, and information of their position with respect to the electrode shaft and of the stimulating electric field to predict the positions of all active axons. **(c)** The VTA is constructed from the predictions of the classifier ( $\pm 3$  V, 90  $\mu$ s, 1000  $\Omega$ , isotropic tissue conductivity).

The reduction in the computational runtime comes from the use of fewer axons in the multicompartiment axon model. Figure 7.11 shows how the simulation runtime grows linearly with the number of sampled

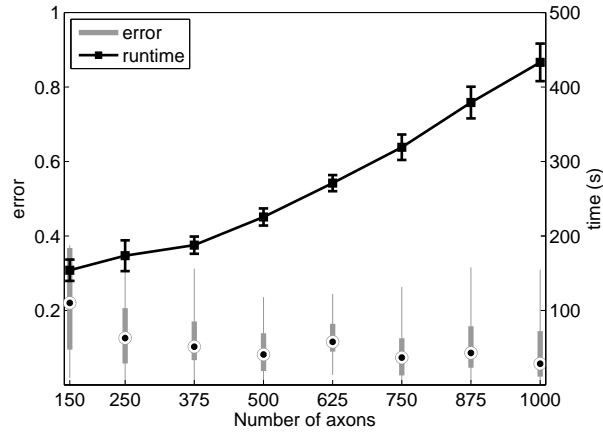


Figure 7.11: Box-whisker plots of the prediction errors and average simulation runtimes (mean $\pm$ SD) as functions of the number of axons used in the classification procedure. The simulation runtime grows in a linear fashion with the number of axons, whereas the median prediction error remains below 0.2 after the number axons exceeds 250.

axons ( $n$ ). These average values were obtained for volumes of tissue activated estimated for 20 randomly selected combinations of stimulation parameters from Table 6.3, assuming either isotropic or anisotropic conductivity conditions, and holding the pulse width at  $90\ \mu\text{s}$ . On the other hand, for the same data set, the prediction errors stabilize after the number of axons reaches 250.  $n = 500$  was chosen to evaluate the performance of the proposed method because it is past that point and falls in the range between 5% and 10% of the total axonal population. The average time to estimate the VTA for all trials and stimulation parameter settings, sampling 500 axons, was 267.7 s. This figure represents a reduction of 92.3% compared with an average time of 3467.9 s required to solve the model described in section 6.1.2 (models running in a Dell optiplex 990 with an Intel Core i7-2600 processor, and 8 GB RAM.).

Activation threshold curves [12, 15] can achieve simulation runtimes of under 1 s, that is, if they are not fitted every time the stimulation parameters vary. Otherwise it is necessary to run full multi-compartment axon models to obtain new data to fit them. Whatever the case, they are prone to error. Figure 7.12 shows the total errors generated by the classifier and by threshold curves with respect to reference data sets for the monopolar configuration and several combinations of stimulation parameters. The Gaussian process emulator easily outperformed the threshold curves, independently of whether isotropic or anisotropic conductivities were assumed, although with larger uncertainties in the latter case. Also, unlike the curves, the proposed emulator allows for the estimation of the VTA when more than one of the electrode contacts are active.

Figure 7.13 shows four different volumes of tissue activated for two different bipolar stimulation parameter settings, but under different conductivity conditions. It displays the ability of the emulator not only to work with multi-contact stimulation, but also to represent the effects that tissue conductivity has on the VTA. The tissue conductivity affects the VTA via changes in the propagation of the stimulus waveform and consequently on axonal activation. The volumes of tissue activated when isotropic conductivity is assumed exhibit radial symmetry with respect to the electrode axis, as expected. Such symmetry disappears for the anisotropic case. In terms of the prediction error, the two bipolar configurations studied, follow

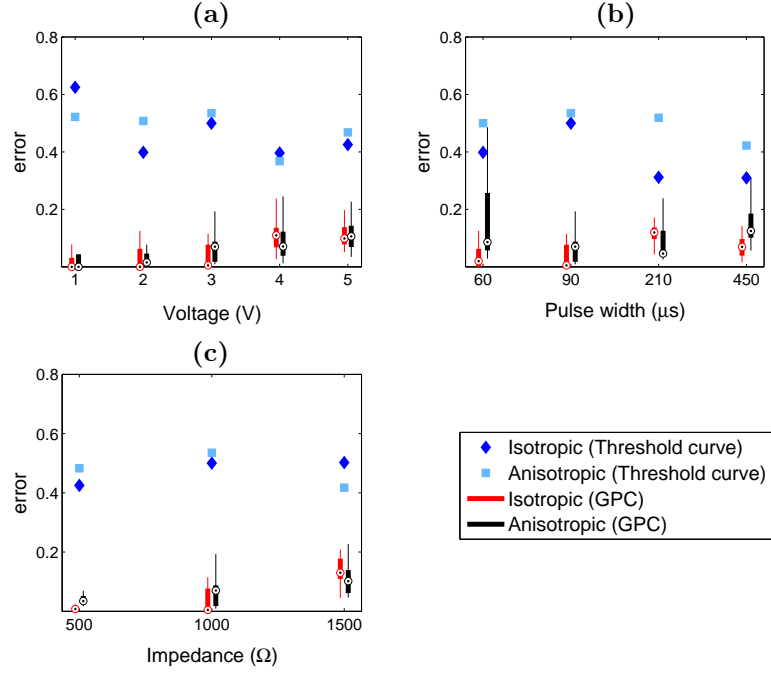


Figure 7.12: Prediction errors for the monopolar configuration: **(a)** amplitude, **(b)** pulse width, and **(c)** impedance variations. The GPC (box-whisker plots) markedly outperformed the activation threshold curves in the range parameter settings studied, regardless of the tissue conductivity conditions considered.

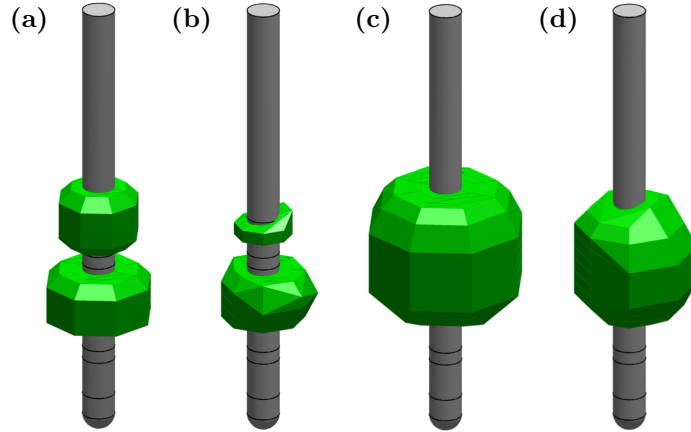


Figure 7.13: Volumes of tissue activated estimated by the classifier for the two bipolar configurations used: **(a)** anode-cathode configuration (bipolar $\{\pm\}$ ) under isotropic tissue conductivity, **(b)** anode-cathode configuration under anisotropic tissue conductivity, **(c)** cathode-cathode configuration (bipolar $\{-\}$ ) under isotropic tissue conductivity, **(d)** cathode-cathode configuration under anisotropic tissue conductivity. As observed the proposed method is able to capture changes in the VTA due to variations in the tissue medium conductivity.

distinct trends (see Figure 7.14). While the error for the cathode-cathode configuration remains low, stable, and with similar differences between the isotropic and anisotropic scenarios across the range of stimulation parameter settings simulated, the error for the anode-cathode configuration is higher and presents large variations between tissue conductivity conditions. Figure 7.15 shows these tendencies more clearly. The error grows with the complexity of the shape of the VTA. Isotropic conductivities give rise to axially symmetric spreads of axonal activation. Tissue anisotropy changes this ideal situation and the median error increases accordingly. But more than the effect of anisotropy, it is having two spatially separate regions of activation what affects the most the performance of our method. Median errors for the anode-cathode configuration, which produces independent volumes of tissue activated for each active contact, double those of the other two configurations. However, even in this worse case scenario, the GP emulator matches the performance of activation threshold curves for the simpler monopolar case.

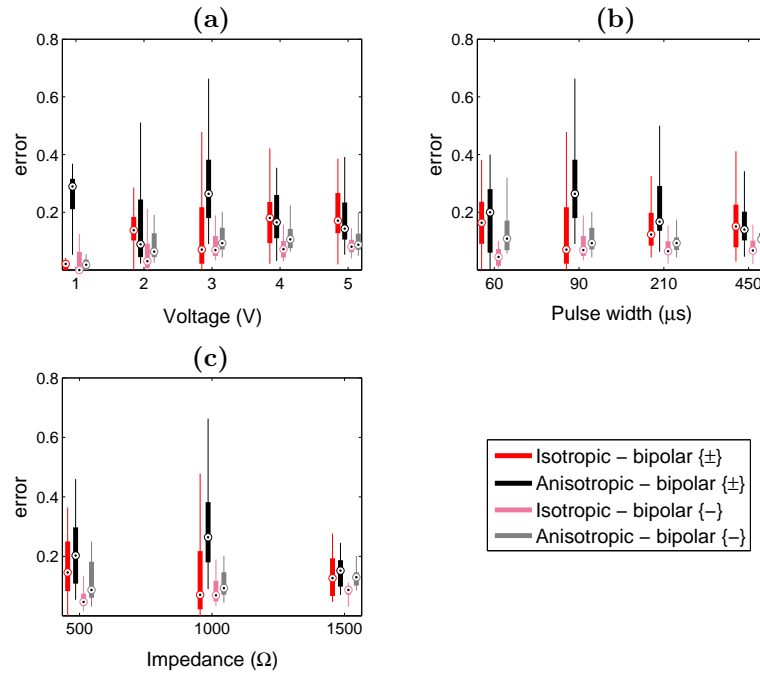


Figure 7.14: Box-whisker plots of the prediction errors for the two bipolar configurations used: **(a)** amplitude, **(b)** pulse width, and **(c)** impedance variations. The performance of the classifier for the cathode-cathode configuration is stable across the range of parameter settings studied, for the cathode-anode configuration larger errors are observed and the difference between the isotropic and anisotropic cases becomes apparent.

A side benefit of the methodology developed in this project is that once trained the classification system allows to make predictions on points in space other than where the axons were built, as long as the electric potential is known at those locations. In other words, the resolution of the VTA no longer depends entirely on the axonal field density (on the space between the axons of the field). Figure 7.16 shows a VTA predicted directly on a FEM mesh. While these smoother VTAs don't provide much new information, they are more convenient for any visualization software.

At this point, we must note that the error metric used to assess the performance of the emulator is geared

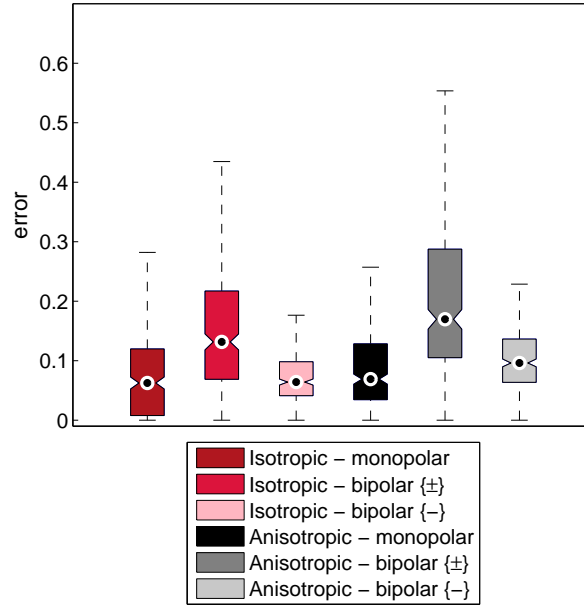


Figure 7.15: Box-whisker plots of the GP classifier prediction errors across all stimulation parameter settings, for the three active contact configurations used, under isotropic and anisotropic tissue conductivity conditions.

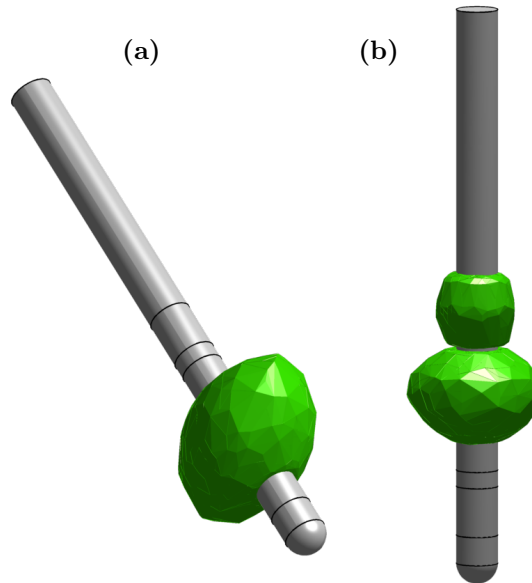


Figure 7.16: **(a)** Monopolar and **(b)** bipolar VTAs predicted directly on a FEM mesh by a trained GP classifier.

towards classification problems, and it is in that sense appropriate for our case. However, it is only partially bounded and more importantly it does not account for the morphology of the VTA. Because of this, we explored an alternative metric, the PMI (positive matching index), a bounded measure of similarity between objects based on lists of their attributes [41]. The PMI gives similarity values between 0 (completely dis-

similar ) and 1 (identical) for the volumes of tissue activated estimated by the classifier and those obtained directly from multi-compartment axon models, instead of an abstract error that can vary between 0 and infinity. However, the qualitative information provided by this similarity measure was the same as that of the initial error metric and we considered that including it in this document would have been redundant. The problem of directly accounting for morphological errors in the estimated VTA, which we think could have more practical meaning, is a pending task and constitutes a future line of work.

A second important point is that our results were obtained applying a single DBS stimulation pulse to the multi-compartment axon models. The VTA criterion is clear in that an axon is considered active if it fires an action potential for each DBS pulse, but there is less clarity about the number of pulses that should be applied to verify that condition. In [4] the authors report that they did not observe any changes in their results after applying a train of 25 DBS pulses to their experimental setting. In [7] the authors used up to 12 in their experiments. In our case, increasing the number of pulses applied to the reference model, described in section 6.1.2, did not produce any observable changes in our results. We then set up a smaller axonal field of 738 fibers arranged as in [9] but with a higher axonal density (0.25 mm separation between axons in the horizontal and vertical directions). This new set up revealed small changes in the periphery of the VTA as the number of applied pulses increased (Figure 7.17). However, the combined effect of increasing the time of simulation, to represent the delivery of a train of pulses, and the number of axons, to obtain the same axonal density in the entire region of interest around the DBS electrode, would result in a disproportional increase in the computational burden compared to the benefits of a more detailed model. Our initial set-up was detailed enough to reproduce successfully experimental results presented elsewhere [7, 9].

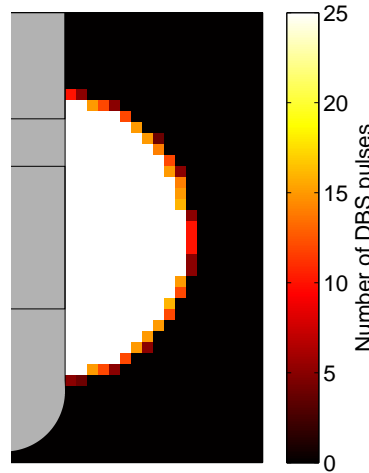


Figure 7.17: Variations in the VTA due to the number of applied DBS pulses used for its estimation.

We must also highlight the fact that the number of parameter settings used in this study is only a small fraction of the thousands of possible combinations of stimulation parameters offered by DBS devices. The proposed methodology is intended to work for any of such combinations, but we chose to focus on the parameter ranges advised in clinical guidelines [42], specially in regard to the stimulation amplitude and to the number of active contacts. Our approach also assumes highly idealized axonal orientations and trajectories. Nonetheless, models based on these simplifications have yielded positive results in studies that compared their predictions of the VTA with experimental data from Parkinson's disease patients implanted

with DBS systems [14]. A last important point is that although the computational runtime of our method is much shorter than that of full multi-compartment axon models, it is still high for real-time applications. Further reductions in the computation time required for VTA estimation can be achieved by optimizing the use of computational resources, e.g., running a version of the code that parallelized the execution of NEURON [43], once per each of the stimulation parameters shown in Table 6.3, reduced the average simulation runtime by an additional 22.6%.

## 8. Conclusions

---

In this project we developed a new methodology to reduce the computation time required to estimate the volume of tissue activated during deep brain stimulation. We built a Gaussian process emulator that combined multi-compartment axon models coupled to the stimulating electric field with a Gaussian process classifier. Our approach cut down to a tenth the average computational runtime of VTA estimation compared with the gold standard. In addition, it allowed for the estimation of the VTA for non-monopolar stimulation, overcoming a limitation of commonly used alternatives, such as activation threshold curves. It also outperformed these, in terms of their prediction errors, for all the combinations of parameter settings studied where direct comparison was possible. Finally, the emulator also succeeded in estimating the VTA when realistic anisotropic brain tissue conductivities were included in the simulation model.

## Bibliography

---

- [1] Jens Volkmann, Jan Herzog, Florian Kopper, and Güntner Deuschl. Introduction to the programming of deep brain stimulators. *Movement disorders*, 17(S3):S181–S187, 2002. 4
- [2] Cameron C McIntyre and Philip J Hahn. Network perspectives on the mechanisms of deep brain stimulation. *Neurobiology of disease*, 38(3):329–337, 2010. 4
- [3] Cameron C McIntyre, Warren M Grill, David L Sherman, and Nitish V Thakor. Cellular effects of deep brain stimulation: model-based analysis of activation and inhibition. *Journal of neurophysiology*, 91(4):1457–1469, 2004. 4, 25
- [4] Svjetlana Miocinovic, Martin Parent, Christopher R Butson, Philip J Hahn, Gary S Russo, Jerrold L Vitek, and Cameron C McIntyre. Computational analysis of subthalamic nucleus and lenticular fasciculus activation during therapeutic deep brain stimulation. *Journal of neurophysiology*, 96(3):1569–1580, 2006. 4, 28, 36
- [5] Rosa Q So, Alexander R Kent, and Warren M Grill. Relative contributions of local cell and passing fiber activation and silencing to changes in thalamic fidelity during deep brain stimulation and lesioning: a computational modeling study. *Journal of computational neuroscience*, 32(3):499–519, 2012. 4, 28, 29, 30
- [6] Merrill J Birdno, Wei Tang, Jonathan O Dostrovsky, William D Hutchison, and Warren M Grill. Response of human thalamic neurons to high-frequency stimulation. *PloS one*, 9(5):e96026, 2014. 4, 25, 28
- [7] Nada Yousif, Nuri Purswani, Richard Bayford, Dipankar Nandi, Peter Bain, and Xuguang Liu. Evaluating the impact of the deep brain stimulation induced electric field on subthalamic neurons: A computational modelling study. *Journal of neuroscience methods*, 188(1):105–112, 2010. 4, 18, 36
- [8] Nada Yousif, Roman Borisyuk, Nicola Pavese, Dipankar Nandi, and Peter Bain. Spatiotemporal visualization of deep brain stimulation-induced effects in the subthalamic nucleus. *European Journal of Neuroscience*, 36(2):2252–2259, 2012. 4
- [9] Christopher R Butson and Cameron C McIntyre. Tissue and electrode capacitance reduce neural activation volumes during deep brain stimulation. *Clinical neurophysiology*, 116(10):2490–2500, 2005. 4, 36
- [10] Christopher R Butson, Scott E Cooper, Jaimie M Henderson, and Cameron C McIntyre. Patient-specific analysis of the volume of tissue activated during deep brain stimulation. *Neuroimage*, 34(2):661–670, 2007. 4

- [11] Cameron C McIntyre, Andrew G Richardson, and Warren M Grill. Modeling the excitability of mammalian nerve fibers: influence of afterpotentials on the recovery cycle. *Journal of neurophysiology*, 87(2):995–1006, 2002. 4, 19, 20, 21, 28
- [12] M Astrom, Elin Diczfalusy, Hubert Martens, and K Wardell. Relationship between neural activation and electric field distribution during deep brain stimulation. *IEEE Trans. Biomed. Eng.*, 62(2):664–672, 2015. 5, 6, 23, 32
- [13] Ashutosh Chaturvedi, J Luis Luján, and Cameron C McIntyre. Artificial neural network based characterization of the volume of tissue activated during deep brain stimulation. *Journal of neural engineering*, 10(5):056023, 2013. 5, 6, 18
- [14] Anneke MM Frankemolle, Jennifer Wu, Angela M Noecker, Claudia Voelcker-Rehage, Jason C Ho, Jerrold L Vitek, Cameron C McIntyre, and Jay L Alberts. Reversing cognitive–motor impairments in Parkinson’s disease patients using a computational modelling approach to deep brain stimulation programming. *Brain*, 133(3):746–761, 2010. 5, 37
- [15] Christopher R Butson and Cameron C McIntyre. Role of electrode design on the volume of tissue activated during deep brain stimulation. *Journal of Neural Engineering*, 3(1):1, 2006. 5, 6, 18, 23, 32
- [16] Leonardo S Bastos and Anthony O’Hagan. Diagnostics for Gaussian process emulators. *Technometrics*, 51(4):425–438, 2009. 5, 15
- [17] Anthony O’Hagan. Bayesian analysis of computer code outputs: a tutorial. *Reliability Engineering & System Safety*, 91(10):1290–1300, 2006. 5, 15
- [18] Bin He. *Neural engineering*, volume 3. Springer Science & Business Media, 2007. 9
- [19] G Bard Ermentrout and David H Terman. *Mathematical foundations of neuroscience*, volume 35. Springer Science & Business Media, 2010. 9
- [20] Robert Plonsey and Roger C Barr. *Bioelectricity: a quantitative approach*. Springer Science & Business Media, 2007. 9, 10, 14
- [21] Alan L Hodgkin and Andrew F Huxley. A quantitative description of membrane current and its application to conduction and excitation in nerve. *The Journal of physiology*, 117(4):500–544, 1952. 11
- [22] David Sterratt, Bruce Graham, Andrew Gillies, and David Willshaw. *Principles of computational modelling in neuroscience*. Cambridge University Press, 2011. 12, 14
- [23] Frank Rattay. Analysis of models for extracellular fiber stimulation. *Biomedical Engineering, IEEE Transactions on*, 36(7):676–682, 1989. 14
- [24] Christopher M Bishop et al. *Pattern recognition and machine learning*. Springer New York, 2006. 15
- [25] Carl Edward Rasmussen and Christopher K. I. Williams. *Gaussian Processes for Machine Learning*. The MIT Press, 2006. 16
- [26] Malte Kuss and Carl Edward Rasmussen. Assessing approximate inference for binary gaussian process classification. *The Journal of Machine Learning Research*, 6:1679–1704, 2005. 16

- [27] Hannes Nickisch and Carl Edward Rasmussen. Approximations for binary gaussian process classification. *Journal of Machine Learning Research*, 9:2035–2078, 2008. 16, 23
- [28] Anastasis C Polycarpou. Introduction to the finite element method in electromagnetics. *Synthesis Lectures on Computational Electromagnetics*, 1(1):1–126, 2005. 17
- [29] Tianhe C Zhang and Warren M Grill. Modeling deep brain stimulation: point source approximation versus realistic representation of the electrode. *Journal of neural engineering*, 7(6):066009, 2010. 18
- [30] Lin-Ching Chang, Derek K Jones, and Carlo Pierpaoli. Restore: robust estimation of tensors by outlier rejection. *Magnetic Resonance in Medicine*, 53(5):1088–1095, 2005. 18
- [31] David S Tuch, Van J Wedeen, Anders M Dale, John S George, and John W Belliveau. Conductivity tensor mapping of the human brain using diffusion tensor mri. *Proceedings of the National Academy of Sciences*, 98(20):11697–11701, 2001. 18
- [32] Ashutosh Chaturvedi, Christopher R Butson, Scott F Lempka, Scott E Cooper, and Cameron C McIntyre. Patient-specific models of deep brain stimulation: influence of field model complexity on neural activation predictions. *Brain stimulation*, 3(2):65–77, 2010. 18
- [33] Cameron C McIntyre and Warren M Grill. Excitation of central nervous system neurons by nonuniform electric fields. *Biophysical journal*, 76(2):878–888, 1999. 19
- [34] Donald R McNeal. Analysis of a model for excitation of myelinated nerve. *IEEE Trans. Biomed. Eng.*, (4):329–337, 1976. 19
- [35] Frank Rattay. Analysis of models for external stimulation of axons. *Biomedical Engineering, IEEE Transactions on*, (10):974–977, 1986. 19
- [36] Grégoire Walckiers. *Bio-electromagnetic model of deep brain stimulation*. PhD thesis, École polytechnique fédérale de Lausanne EPFL, 4 2009. 20
- [37] Michael L Hines, Andrew P Davison, and Eilif Muller. Neuron and python. *Frontiers in neuroinformatics*, 3, 2009. 20
- [38] Michael L Hines and Nicholas T Carnevale. The neuron simulation environment. *Neural computation*, 9(6):1179–1209, 1997. 20
- [39] Merrill J Birdno and Warren M Grill. Mechanisms of deep brain stimulation in movement disorders as revealed by changes in stimulus frequency. *Neurotherapeutics*, 5(1):14–25, 2008. 29, 30
- [40] Jonathan E Rubin, Cameron C McIntyre, Robert S Turner, and Thomas Wichmann. Basal ganglia activity patterns in parkinsonism and computational modeling of their downstream effects. *European Journal of Neuroscience*, 36(2):2213–2228, 2012. 30
- [41] Daniel Andrés Dos Santos and Reena Deutsch. The positive matching index: A new similarity measure with optimal characteristics. *Pattern Recognition Letters*, 31(12):1570–1576, 2010. 35
- [42] American Association of Neuroscience Nurses. Care of the movement disorder patient with deep brain stimulation. AANN Clinical Practice Guideline Series, 2009. 36
- [43] Michael L Hines and N Ted Carnevale. Translating network models to parallel hardware in neuron. *Journal of neuroscience methods*, 169(2):425–455, 2008. 37